

Flares in Open Clusters with K2.

II. M35, Hyades, and Ruprecht 147

Ekaterina Ilin¹, Sarah J. Schmidt¹, Katja Poppenhäger¹, James R. A. Davenport² and Klaus G. Strassmeier¹

¹ Leibniz Institut für Astrophysik Potsdam
e-mail: eilin@aip.de

² University of Washington e-mail: jrad@uw.edu

Received XXX; accepted XXX

ABSTRACT

Context. Flares can help us trace magnetic activity because are bright and high-contrast on low mass stars.

Aims. This study aims to quantify flaring activity on these stars as a function of mass and age.

Methods. We automatically detected flares in K2 time-domain photometry, using the open-source software K2SC to remove instrumental and astrophysical variability from K2 light curves. We used injection and recovery of synthetic flares to assess detection thresholds, time sampling and de-trending effects on the inferred flare energies. With additional data from the full K2 archive we added stars with a larger variety of ages and spectral types to the analysis of the previous study (Ilin et al. 2019). We compared previous results from the Pleiades and Praesepe to the flare frequency distributions (FFDs) in M35 and the Hyades, respectively. Ruprecht 147 filled in the age gap at 2.5 Gyr between the aforementioned young clusters and the solar age cluster M67.

Results. We find that the flare production mechanism is similar for the entire parameter space, following a power law relation with exponent $\alpha \approx 2$, but the flaring frequencies depend on both mass, and age. We discuss X and Y.

Key words. Methods: data analysis, Stars: activity, Stars: flare, Stars: low-mass

Use \titlerunning to supply a shorter title and/or \authorrunning to supply a shorter list of authors.

1. Introduction

Flares are explosions on stellar surfaces with a complex spatial and temporal and energetic phenomenology. We know that flares are magnetic re-connection events that lead to a change in field line topology and subsequent energy release (Priest & Forbes 2002). We can observe flares in nearly all electromagnetic bands, from radio to X-rays, and on all stars that possess a convection zone, from late F type stars to ultracool dwarfs (Gizis 2013). But even with continuous monitoring at high temporal resolution, the random occurrence of solar flares makes them costly observing targets, especially in coordinated multi-band observations. In integrated light, most solar flares have a far too low contrast and intensity to be observable. Stellar flares on cool stars have two advantages in this respect. They are often bright, enhancing stellar flux by up to several orders of magnitude, and they typically exhibit blackbody emission at temperatures significantly higher than their stars' photospheres.

With the evidence that the physical processes that cause flares on the Sun and other stars are the same (Karooff 2016), solar and stellar flares can inform each other (Shibayama et al. 2013). Inconsistencies in extrapolations from solar to stellar conditions (Aarnio et al. 2011; Aarnio et al. 2012; Drake et al. 2013) provide valuable clues to the differences in magnetic properties between Sun and M dwarfs, too (Alvarado-Gómez et al. 2018). Large surveys like Kepler and TESS enable statistical flare studies of stars that were not pre-selected for their activity (Walkowicz et al. 2011). Statistical studies of stellar flaring activity can help us understand the underlying physical processes CITE stellar surface magnetic fields, starspots (Davenport 2015; Howard

et al. 2019b), how flares relate to stellar angular momentum evolution (Mondrik et al. 2019; Howard et al. 2019b), how they affect the atmospheres of exoplanets (Lecavelier des Etangs et al. 2012; Loyd et al. 2018; Tilley et al. 2019; Howard et al. 2019a), and inform galactic archaeology (Howard et al. 2019a).

Basic parameters that affect flaring behaviour on stars are their masses, and ages. Ages can be controlled for in coeval groups of stars, and flaring-age studies in binaries showed consistency in activity for both components in the majority of targets (Lurie et al. 2015; Clarke et al. 2018). Open clusters present other coeval groups of stars with well-determined ages. Ilin et al. (2019) (hereafter PaperI) investigated the flaring activity of late-K to mid-M dwarfs in three open clusters (OCs), the Pleiades, Praesepe, and M67, using K2 time domain photometry. They analysed the flare frequency distributions (FFDs), with respect to different masses and cluster ages. For the cluster members, the light curves revealed that their flaring activity declines both with age and mass. The decline is faster for higher mass stars. Recently, Davenport et al. (2019) put forward an empirical parametrization of this flaring-mass-age relation based on FFDs. The present study aims to extend the results in PaperI to the age of Ruprecht 147 (2.5 Gyr), and both higher and lower masses than in the previous study. We also test the previous results from the Pleiades on M35, and the results from Praesepe on the Hyades, as both OC pairs have approximately the same ages. Because the Kepler satellite retired in fall 2018, we can now use the complete K2 data set, and supplement all three OCs in PaperI with additional light curves. Additionally, we use high quality K2 light curves available for M67 (Nardiello et al. 2016) and M35 (Soares-Furtado et al. 2017). We discuss our results with

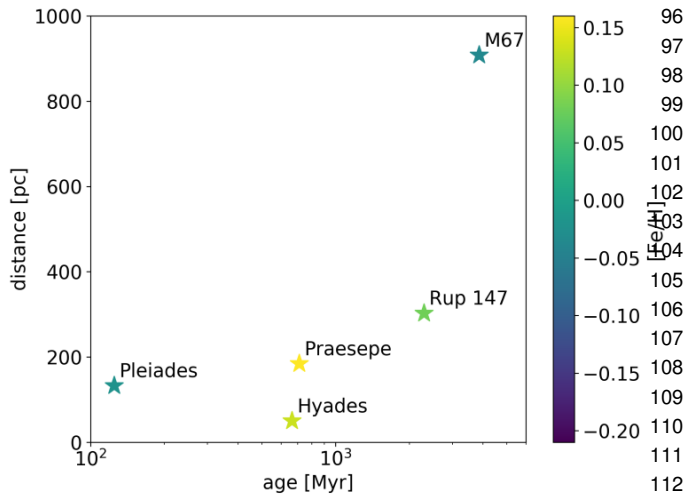


Fig. 1. The values for age, metallicity, and distance are approximate values from a compilation of existing literature, see Appendix B.1.

respect to potential breaks in the power law distribution at high energies. Finally, we use the results to test the parametrization in Davenport et al. (2019).

2. Data

Our main data are K2 target pixel files that were provided by the Kepler archives hosted at MAST, and light curves derived from them (Aigrain et al. 2016; Soares-Furtado et al. 2017; Vinícius et al. 2018). To assign T_{eff} to the targeted stars we used multi-band photometry obtained from Tycho, UCAC4, 2MASS, Pan-STARRS, and Gaia catalogs. To assign ages to the targeted stars, OC membership information was compiled from the literature. An overview over the cluster sample is presented in Table ?? and illustrated in Figure 1.

2.1. K2 light curves

The Kepler (Koch et al. 2010) spacecraft finished its follow-up mission K2 (Howell et al. 2014) in September 2018, after having completed nearly 20 80-day observing campaigns. Even though Kepler and K2 data are used in more than 2 400 publications to date, the public archive can still be considered understudied (Bastien et al. 2018). In this spirit we took up the analysis of about 4 000 Kepler target pixel files that each contain up to 80 days of minimum cadence observations in white light (4,200 – 9,000 Å). We also used light curves extracted from the K2 C0 super stamps. A super stamp is an aggregated set of typical Kepler postage stamps placed over a densely populated field, that also covers M35 (Soares-Furtado et al. 2017). As K2 was conducted on the two-wheeled Kepler satellite, it was subjected to substantial drift motion (spacecraft roll, Van Cleve et al. 2016) and had an overall reduced pointing accuracy. To mitigate these effects, various solutions were developed (Vanderburg & Johnson 2014; Aigrain et al. 2016; Luger et al. 2018).

2.2. Membership matching

We obtained membership information from multiple catalogs for each cluster. We cross-matched these catalogs on RA and

declination within 3 arcsec. The resulting target lists were used to search the K2 archive, or were matched to the catalogs of extracted light curves from crowded fields in the case of M35 (Soares-Furtado et al. 2017) and M67 (Nardiello et al. 2016).

One part of the membership catalogs provided membership probabilities (Douglas et al. 2014; Bouy et al. 2015; Cantat-Gaudin et al. 2018; Olivares et al. 2018; Reino et al. 2018; Gao 2018; Olivares et al. 2019). For the other part no probability was provided (Rebull et al. 2016a; Douglas et al. 2017; Gaia Collaboration et al. 2018a), or qualitative classifiers were given (Curtis et al. 2013; Gonzalez 2016; Rebull et al. 2017). In the latter cases we assigned approximate probabilities anchored to the set threshold for inclusion into our final sample. Absence in a catalog did not decrease the likelihood of membership, as each catalog shows different selection biases which we did not address in this study. We set the threshold mean membership probability p for a target in our sample to 0.8.

2.3. Open Clusters

We studied flaring activity in the low mass stars in six open clusters spanning from ZAMS to solar age. Table 1 provides an overview over the final sample. The literature overview of age, distance, and metallicity determinations is given in Table ?? in the Appendix. Membership probability histograms of the final sample are displayed in Figure ??.

2.3.1. Pleiades

The Pleiades, a nearby ZAMS cluster, were observed in Campaign 4, and were treated in Paper I. We include the cluster in this work for completeness and to illustrate improvements to (Paper I). We revisited the memberships from Rebull et al. (2016a), which were used in the previous work, and merged them with lists of members determined by Olivares et al. (2018); Gaia Collaboration et al. (2018a); and Cantat-Gaudin et al. (2018).

2.3.2. M35

M35 is a ZAMS cluster 900 pc away, observed during Campaign 0 in K2. We merged membership lists from Cantat-Gaudin et al. (2018); Gaia Collaboration et al. (2018a); and Bouy et al. (2015). There are only five K2 light curves, but we identified multiple additional members with publicly available¹ light curves obtained from Soares-Furtado et al. (2017). They used an image subtraction technique in the campaign's super stamps, a self flat-fielding de-trending inspired by K2SFF (Vanderburg & Johnson 2014), and a trend-filtering algorithm developed by Kovács et al. (2005). We preferred PSF photometry in cases where both aperture K2 and PSF LCs were available. We took the raw extracted PSF light curves and de-trended them using K2SC.

2.3.3. Hyades

The Hyades are a 0.6 Gyr old OC observed during Campaigns 4 and 13 with K2. It is about as old as Praesepe. We merged membership tables obtained from Douglas et al. (2014); Reino et al. (2018); and Gaia Collaboration et al. (2018a).

¹ <https://k2.hatsurveys.org/archive/>

Table 1. Open clusters.

| | d [pc] | stars | LCs | flares | campaigns | age [Myr] | [Fe/H] |
|----------|--------|-------|-----|--------|-----------|-------------------------|-------------|
| Pleiades | 135.6 | 761 | 761 | 1606 | 1 | 135 $^{(25)}_{(25)}$ | −0.04(0.03) |
| Hyades | 46.0 | 171 | 171 | 396 | 2 | 690 $^{(100)}_{(160)}$ | 0.13(0.02) |
| Praesepe | 185.5 | 964 | 964 | 906 | 3 | 750 $^{(7)}_{(3)}$ | 0.16(0.00) |
| Rup 147 | 305.0 | 53 | 53 | 9 | 1 | 2650 $^{(380)}_{(380)}$ | 0.08(0.07) |
| M67 | 908.0 | 307 | 307 | 1 | 3 | 3639 $^{(17)}_{(17)}$ | −0.10(0.08) |

Notes. n is the approximate number of members with $p > 0.8$. LCs, SLCs, LLCs, and PSF LCs denote the number of available light curves, short cadence light curves, long cadence light curves, and PSF de-detrended light curves, respectively. The values for age, [Fe/H], and distance are approximate values from a comparison of existing literature, detailed in Appendix B.1.

2.3.4. Praesepe

Praesepe appeared in Campaign 5, and was previously treated in Paper I. It was then observed again during Campaign 13. We revisited the memberships obtained by Douglas et al. (2014), and matched them to the members identified in Douglas et al. (2017); Rebull et al. (2017); Cantat-Gaudin et al. (2018); and Gaia Collaboration et al. (2018a).

If an extinction value was not available for a given star we used the average extinction value of the respective cluster. We accounted for extinction in Gaia BP and RP using the reddening $E(B_p - R_p)$ derived from Gaia photometry and parallax from Gaia DR2 (Andrae et al. 2018). We dropped targets that were too bright (Kepler magnitude $K_p \leq 9$).

2.3.5. Ruprecht 147

Ruprecht 147 is a 2.5 Gyr old OC observed during Campaign 7 with K2. We used the mean membership probabilities obtained from a number of studies (Curtis et al. 2013; Cantat-Gaudin et al. 2018; Olivares et al. 2019) combined with the members found by Gaia Collaboration et al. (2018a) to identify the most likely members.

2.4.2. Effective temperatures

We applied several methods and color-temperature relations (CTRs) to determine robust T_{eff} . We used CTRs from Boyajian et al. (2013) and Mann et al. (2016) (erratum to Mann et al. 2015), and T_{eff} derived from Gaia DR2 using the StarHorse algorithm (Queiroz et al. 2018) and inferred from Gaia DR2 using the Apsis pipeline (Bailer-Jones et al. 2013; Andrae et al. 2018). Boyajian et al. (2013) determined CTRs from a range of interferometrically characterized stars using $g - z$, $g - i$, $g - r$, $g - J$, $g - H$, and $g - K$ colors from SDSS and Johnson magnitudes for A to K stars. Their sample is centered on solar metallicity, so we contained the use of these CTRs to stars with $-0.25 < [\text{Fe}/\text{H}] < 0.25$. We transformed 2MASS JHK to $J - H$, $H - K$, and $J - K$ in the Johnson system as the authors from 2MASS to the Bessell-Brett system (Carpenter 2001), and from Bessell-Brett to Johnson using the relations in Bessell & Brett (1988).

Mann et al. (2015) provide CTRs from absolutely calibrated spectra to which they fitted atmospheric models to obtain T_{eff} . Alternatively, they determined T_{eff} from long-baseline optical interferometry measurements using the bolometric flux. Among others, they note transformations for SDSS/2MASS $r - z$ and $r - J$, or Gaia $BP - RP$ where extra information can be added from metallicity or 2MASS $J - H$. The relations in Mann et al. (2015) are only valid if metallicity is sufficiently close to solar, which is satisfied for all clusters in this paper (see Table ??). M35 may be an exception to this rule.

We supplemented our estimates with T_{eff} estimates from Anders et al. (2019) who used the StarHorse pipeline (Queiroz et al. 2018) on Gaia DR2.

Gaia DR2 published effective temperatures for over 160 million sources (Gaia Collaboration et al. 2018b). The typical uncertainty is quoted at 324 K, but it is lower for stars above ~ 4100 K and below ~ 6700 K, so that we adopt 175 K which is above the quoted root-median-squared error in this T_{eff} range (Andrae et al. 2018), and use provided values only in this range.

Empirical CTRs suffer from systematic errors that stem both from the different methods applied, and from sample selection biases. We used as many empirical relations as possible in their appropriate ranges to obtain multiple T_{eff} estimates from which

2.4. Effective temperatures, stellar radii, and luminosities

2.4.1. Photometry and extinction correction

We determined effective temperatures T_{eff} using broadband photometry the Two Micron All Sky Survey (2MASS; Skrutskie et al. 2006), the Panoramic Survey Telescope and Rapid Response System (Pan-STARRS) Data Release 1 (Chambers et al. 2016), and Gaia DR2 (Gaia Collaboration et al. 2018b). We applied quality cuts to 2MASS, Pan-STARRS DR1, and Gaia DR2 data, as described in Appendix C, and removed foreground stars using Gaia DR2 parallaxes. We corrected the 2MASS and PanSTARRS photometry in M35, M67, and Ruprecht 147 for extinction using the most recent version (Green et al. 2019) of the `dustmaps` package that provides 3D dust maps derived from 2MASS and PanSTARRS photometry together with Gaia distances (Green et al. 2018). If there was no Gaia parallax available we used the cluster median distance instead

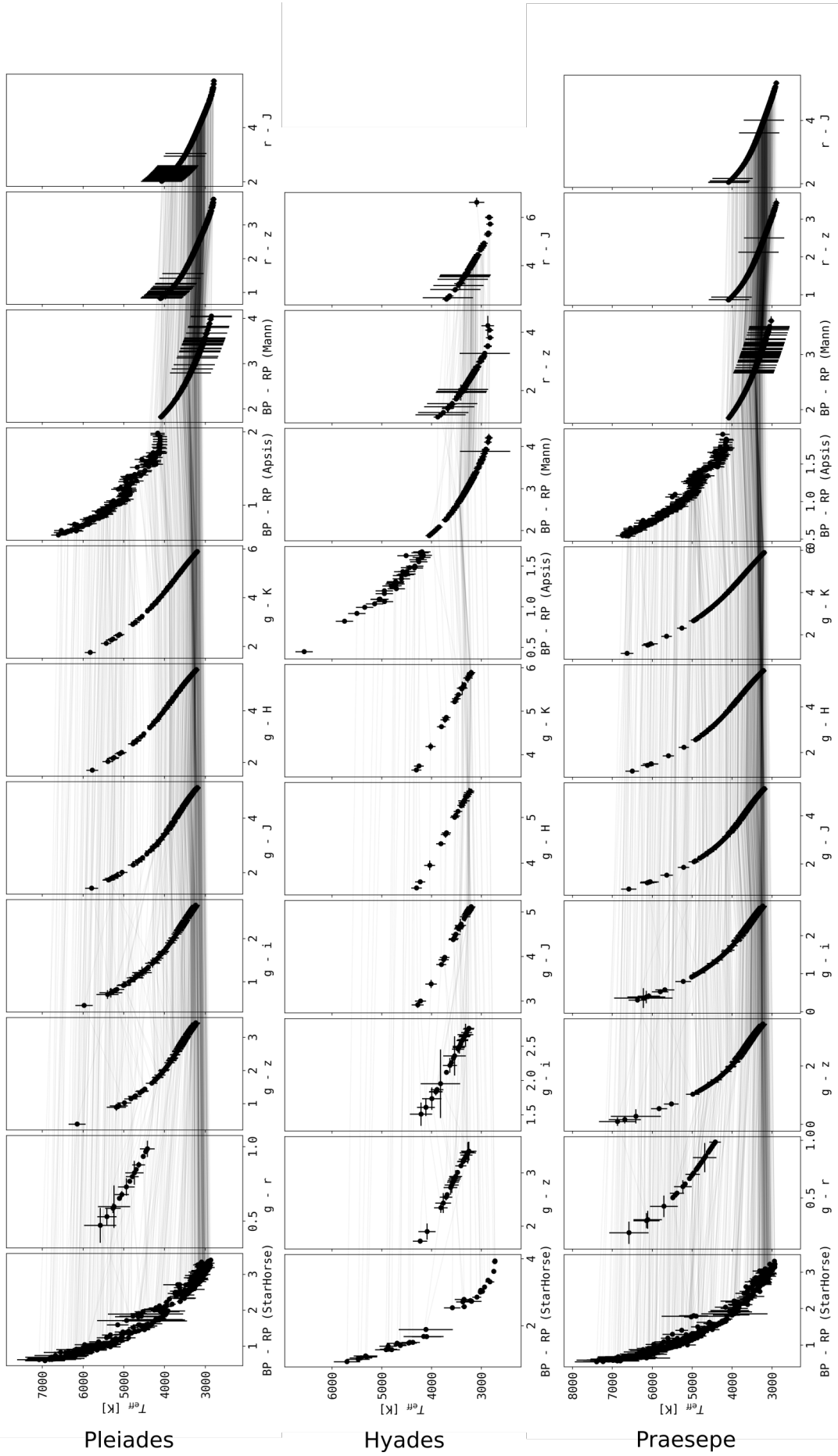


Fig. 2. Color-temperature relations for Pleiades, M35, and Hyades.

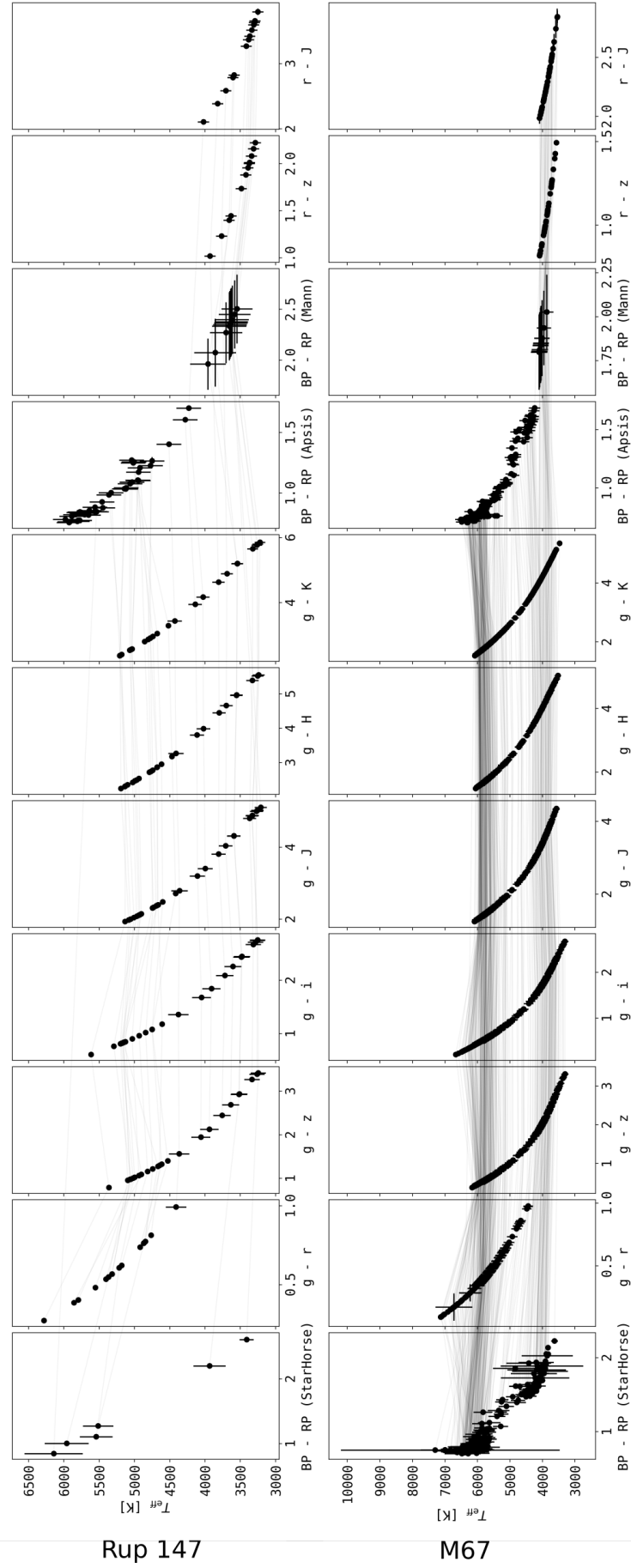


Fig. 3. Color-temperature relations for Praesepe, Ruprecht 147, and M67. Description as in Fig. 2.

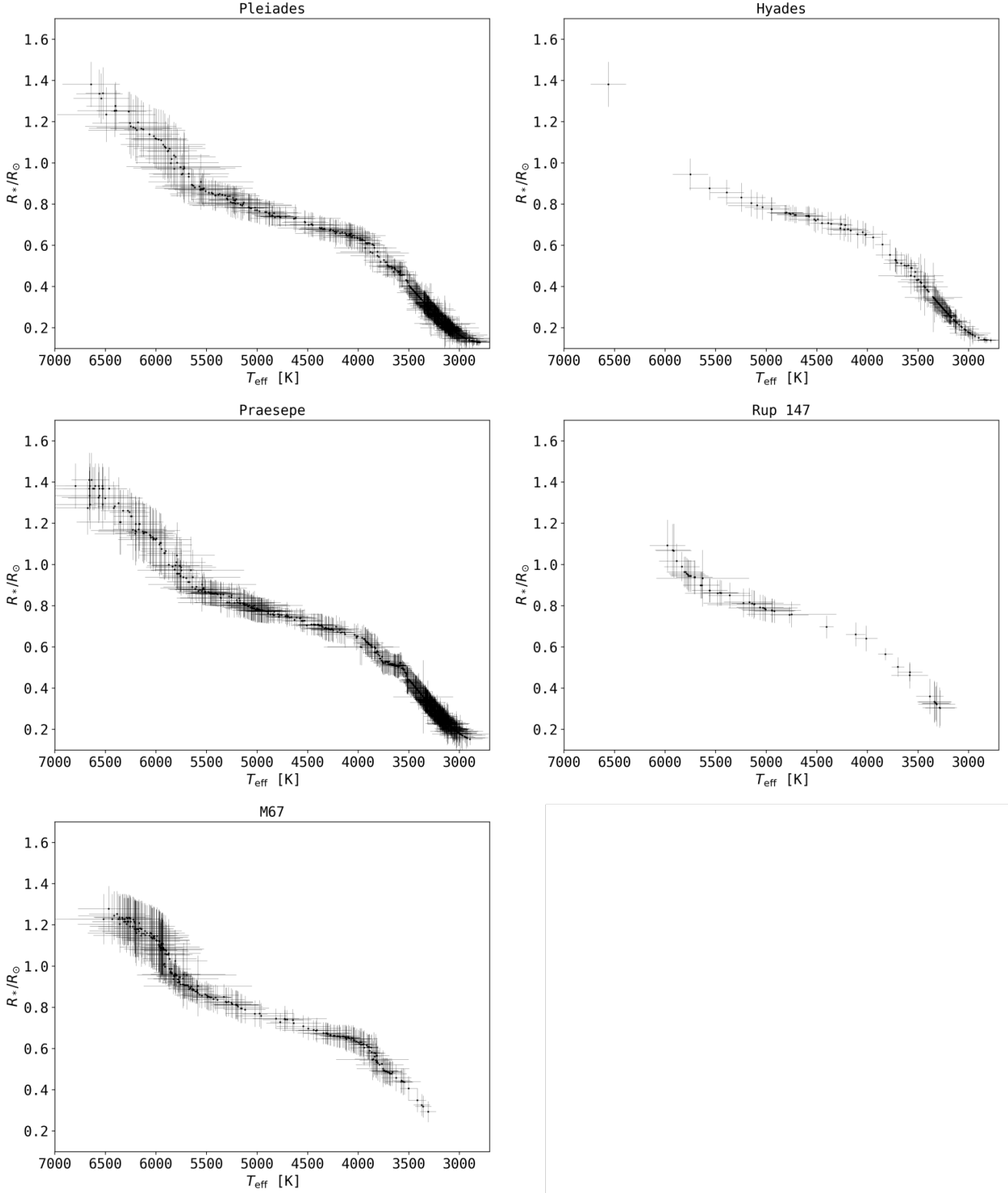


Fig. 4. $T_{\text{eff}} - R_*$ relation for all clusters in this study.

we then drew a more reliable median value. Targets that were lacking sufficient photometric data to derive T_{eff} , or were too hot to be expected to have a convective envelope ($T_{\text{eff}} \geq 7000\text{K}$), were flagged accordingly, and removed from the sample. We dropped all targets where the uncertainty on the weighted mean

T_{eff} was greater than 10%. Only targets that were assigned a T_{eff} were searched for flares.

2.4.3. Stellar radii

We used a catalog of empirically characterised stars (Yee et al. 2017) to derive R_* from T_{eff} (Fig. 4). Yee et al. (2017) collected 404 stars with high-resolution spectra from the literature, and own observations of mid to late K-dwarfs, spanning low mass stars from 7000 K down to 3000 K. For these stars, the resulting catalog is accurate to 100 K in T_{eff} , 15 % in R_* , and 0.09 dex in [Fe/H]. We interpolated between stars from the catalog to our derived T_{eff} , and propagated the resulting scatter to the uncertainty in R_* if $T_{\text{eff}} > 3500$ K. For stars with $T_{\text{eff}} < 3500$ K we used $T_{\text{eff}} - R_*$ relations derived by (Mann et al. 2015, 2016).

2.4.4. Spectra

We assigned spectra to our targets from the SpecMatchEmp Yee et al. (2017) and the FlareSpecPhot libraries (Schmidt 2014; Kirkpatrick et al. 2010; Burgasser et al. 2007, 2008, 2010, 2004; Cruz et al. 2004; Burgasser & McElwain 2006; Rayner et al. 2009; Doi et al. 2010; Filippazzo et al. 2015; Cruz et al. 2003; West et al. 2011; Bochanski et al. 2010, 2007; Schmidt et al. 2010, 2015, 2014; Mann et al. 2015). When a spectrum was available for the derived spectral type in FlareSpecPhot, we preferred it over SpecMatchEmp, which was the case for all stars cooler than M0, where we mapped spectral type to effective temperature as appears in Pecaut & Mamajek (2013). We then combined stellar radii R_* , T_{eff} , and spectra to projected bolometric luminosities $L_{\text{bol},*}$, and projected luminosities in the Kepler band $L_{\text{Kp},*}$ (Shibayama et al. 2013; Ilin et al. 2019). Uncertainties in $L_{\text{Kp},*}$ ranged from 9 % to 52 % with a median value of 17 %.

3. Methods

We detected flare candidates automatically, and validated them by eye. We attempted to assign recovery probabilities and corrected for sampling effects using injection/recovery tests but the procedure was not scalable due to computational costs. We performed injection recovery on a handful of example light curves to see that de-trending and intrinsic light curve properties smear out the ED recovery with varying distributions that add an uncertainty of about 30%. Most of the candidates are expected to have a complex shape that deviates from the classical flare template. The validation yielded an estimate on the uncertainty on the flare energy released in the Kepler band. The frequency distributions of these flare energies are believed to follow a power law that spans multiple orders of magnitude. We adopted this model, and used two different Maximum Likelihood estimators to obtain power law exponents. We tested the best fit parameters with the Kolmogorov-Smirnov test, and probed possible truncation of the power law relation with an exceedance test.

3.1. Flare finding

We used the open source software AltaiPony² to automatically detect and characterize flares in our sample. The code base relies on K2SC³ (Aigrain et al. 2016) to remove instrumental and astrophysical variability from K2 light curves. We did not use the pre-detrended light curves available on MAST, but used K2SC to de-trend light curves from the re-processed final data release. We clipped outliers at 3σ iteratively, as compared to the original work, where outliers were clipped at 5σ (Aigrain et al. 2016).

After de-trending, the flare finder algorithm looked for continuous observing periods, defined as being longer than 10 data points at a minimum cadence of 2 h. All further routines were run on these observing periods. The finder iteratively clipped excursions from the median value at 3σ rolling window noise above median plus uncertainty given from K2SC de-trending. After each iteration, outliers were cut down to the current median value. Either after convergence, or 50 iterations, the resulting median value was adopted. With this median as quiescent flux, flare candidates were identified with the same procedure as during the median value calculation, but now we additionally required at least three consecutive data points to fulfill the 3σ -criterion. Flare candidates were merged into single candidate events if they were less than four data points apart. For each of these candidates flaring time, amplitude and equivalent duration (ED) were returned.

ED is the area between the LC and the quiescent flux, that is, the integrated flare flux divided by the median quiescent flux F_0 of the star, integrated over the flare duration (Hunt-Walker et al. 2012):

$$ED = \int dt \frac{F_{\text{flare}}(t)}{F_0}. \quad (1)$$

ED is a quantity independent of calibration and distance that is suited to compare flaring activity on stars where these properties are uncertain. ED describes the time during which a star releases as much energy as the flare itself. This time can be shorter or longer than the actual flare duration.

The uncertainty in ED depends on the light curve noise properties, time sampling, and other intrinsic characteristics. Moreover, K2SC de-trending and the flare finding procedure introduce additional uncertainty that dominates the photometric noise. Carrying out injection and recovery that takes into account the effect of GP regression that underlies K2SC. We only performed injection-recovery on a small number of light curves with flares to estimate the.

The Kepler flare sample has shown to be difficult to treat in a fully automated way. Without manual vetting, the event samples remain significantly contaminated (Yang & Liu 2019). As K2 was subject to further technical difficulties, the expected contamination rate was expected to be even higher. Some light curves could not be de-trended using K2SC alone. Light curves with extreme astrophysical signals like deep transits, rotational modulation on time scales of a few hours or passages of bright SSOs had to be masked accordingly or fitted with an additional sinusoidal component to the K2SC-treated time series. A number of light curves were excluded from the flare search because they saturated the detector, or because the target aperture overlapped with broken pixels. Some very faint targets and extreme variables could not be searched because the de-trending did not terminate successfully.

Table includes

3.2. Kepler flare energies

(see Paper I for details).

Multiband time resolved observations of active M dwarfs have shown that continuum flux accounts for the majority of the energy radiated by flares (Kowalski et al. 2013). The effective temperature of this blackbody, however, varies by a great degree, with, to date, no robust predictor of that temperature:

While solar flares are relatively cool, with

² <https://github.com/ekaterinailin/AltaiPony>

³ <https://github.com/OxES/k2sc>

$T_{\text{eff}} \approx 5000 - 7000$ K (Kleint et al. 2016; Kerr & Fletcher 2014; Watanabe et al. 2013; Namekata et al. 2017), SEDs of stellar flares tend to be blue (?). At least one M dwarf flare reached 40 000 K as seen in FUV spectra (Froning et al. 2019), and most events exhibit temperatures of about 9 000 – 10 000 K (Hawley & Fisher 1992; Kretzschmar 2011; Shibayama et al. 2013). A dependence of flare temperature on stellar age, or mass, or both, will enter our analysis if we attempt to quantify bolometric flare energy. At about 6 200 K, the Kepler pass band captures the largest flux fraction, at 10 000 K 72 % at 40 000 K only 4% of this value is transmitted. Another effect is that flares of equal flare energy but hotter SED would not be seen in the Kepler band at all. We propagated the uncertainties σ_{ED} and σ_L (on $L_{*,Kp}$) in quadrature to $E_{Kp,flare}$.

3.3. Power law fits

Flare frequency distributions follow power law relations that cover several orders of magnitude, from solar microflares to stellar superflares. We fitted power law functions to the FFDs using three different approaches. The first method was a maximum likelihood estimator (MLE) (Maschberger & Kroupa 2009). As recommended by Maschberger & Kroupa (2009), we applied the stabilized Kolmogorov-Smirnov (KS) test at 95 % significance level to all power law fits in the sample. If the test fails the power law model does not fit the data at the given significance level. If the test passes, this does not give any information whether the power law model is the correct assumption. The goodness of fit can be estimated from the visual inspection of percentile-percentile plots, given in the online material⁴. We used the KS test iteratively to determine the FFDs' low-energy cutoff ED_{\min} for the power law distribution. This cutoff does not reflect the physical threshold for criticality because the cutoff is seen at lower energies in similar stars with higher sensitivity, for example, higher cadence. The cutoff also does not directly imply that flare candidates detected above or below the cutoff are more or less likely to be detected because the flare detection probability is a function of both duration and amplitude, and not only of energy. Above all, it is not straightforward to account for the deviation from an ideal power law at low energies, because the aforementioned effects may be partly cancelled by background contamination from, for instance, cosmic rays (?). We believe that they are mostly limited by the non-linear dependence for the energy bias from time sampling effects (?) and recovery probability of flare duration and amplitude. These parameters are not resolved in FFDs, and while they are correlated there is significant spread in the duration-amplitude relation to blur the cutoff in the FFD. One way to account for this circumstance is to inject and recover synthetic flares with a variety of durations and amplitudes and determine energy ratios and recovery probabilities for each individual candidate, assuming that the underlying flare shape can be sufficiently well parametrized, as was done in Davenport et al. (2014). The second method used the MLE result as a prior for α . Following Wheatland (2004), we defined the joint posterior distribution for the probability ϵ that a flare with ED or energy above some

value S_2 occurs within a time period ΔT :

$$p(\epsilon, \alpha) = C \cdot (-\ln(1 - \epsilon))^M \cdot (\alpha - 1)^M \cdot \Gamma(\alpha) \left[\frac{(S_2/S_1)^{M+1}}{\pi} \right]^\alpha \cdot (1 - \epsilon)^{(T/\Delta T) \cdot (S_2/S_1)^{\alpha-1} - 1}. \quad (2)$$

C is the normalisation constant, M is the number of events, T the total observation time. Γ contains the prior distribution for α , and S_1 denotes the detection threshold above which all flares are detected. π encapsulates the flare energies as

$$\pi = \prod_{i=1}^M \frac{s_i}{S_1} \quad (3)$$

, where $\{s_1, s_2, \dots, s_m\}$ are the flare energies or ED .

The posterior distribution in Wheatland (2004) captures both the Poissonian distribution of flare events in time, and their power law distribution in energy, simultaneously. Wheatland (2004) derived this model to be able to predict the flaring rate of a given active region on the sun, and offered an extension to Eq. 2 that treated changing flaring activity rates as the active region evolves, and also characteristics of the active region itself, such as sunspot classifiers. In our simplification of the model, we assumed that the flare generating process did not change within the observation time span in any star in our sample ($M = M'$ in Eq. 24 in Wheatland (2004)). Another assumption was that this process was the same for all stars in the sample ($\Lambda_{MC} = 1$ in Eq. 24). Under these assumptions the information gained from the light curves could be stacked together.

With a uniform prior for α the results from the MLE and Markov Chain Monte Carlo (MCMC) sampling from the posterior distribution are the same, the latter allowed us to fit for ϵ and α simultaneously. Another advantage of the latter approach is that we could use more informative priors.

We chose our prior to reflect the power law exponent results discussed in the literature. The studies we took into account analysed flare frequency distributions of stellar flares in the optical regime, and focused mostly on K and M dwarfs (Lurie et al. 2015; Howard et al. 2019a; ?; ?) or ultra-cool dwarfs (?) but also solar-type stars (Shibayama et al. 2013). We also used a Gaussian fit to α obtained from the posterior distribution using the full sample of flares as the prior for a subsequent Bayesian analysis of individual age and T_{eff} bins. Assuming that α is universal for all spectral types, ages, and flare energy ranges, we used this more informative, Gaussian prior to further constrain the flaring rates.

Additionally we calculated the exceedance statistic tr to test if the power law distribution was truncated. If tr is 1, the power law distribution is truncated at the high energy end. If tr is 0, no information was gained from the calculation. To derive tr , given a number n of observations X_n and a best fit value for the power law exponent, we generated 500 samples with n values from this best-fit distribution assuming no truncation, i.e. choosing an upper limit several orders of magnitude higher than X_{\max} . We then proceeded to truncate the samples at thresholds T below the maximum observed value X_{\max} and determined the average number N_{ex} of generated values that will exceed T . If the underlying power law is not truncated, N_{ex} declines with larger n , as larger X_{\max} will be present in the original data. If the best fit power law exponent is steeper, N_{ex} will be underestimated. If the best fit power law exponent is flatter, N_{ex} will be overestimated. If the power law is not truncated, for $n \geq 100$ N_{ex}/n will be $< 5\%$, for $20 < n < 100$, typically

⁴ <https://github.com/ekaterinailin/flares-in-clusters-with-k2-ii>

$N_{ex}/n < 15\%$.

4. Results

Fig. ?? shows the $E_{Kp,flare}$ and ED detection thresholds, as defined by the recovery probability (see Sec. ??). The thresholds in ED reflect the noise level in the light curves.

4.1. Flaring activity as a function of a age and T_{eff}

Flaring activity decays with age. Flaring fraction was observed to decline with galactic latitude for M dwarfs (Hilton et al. 2010) Howard+2019. Short rotation periods and high magnetic activity measured in $H\alpha$ are strongly correlated (West et al. 2015). According to gyrochronology, fast rotation indicates young age (Barnes 2003), and slows down as the star ages. Here we quantify how this decline unfolds for different spectral types. Except for the stars in our coolest temperature bin (M5.5–M8, 2 500–3 000 K), stellar flaring activity at a given age is always stronger for a cooler star. The exception is seen at cluster ages around 120 Myr. What creates the strong emission in white light? Extended flare loops, maybe (?)

4.2. M67 and Rup 147

We found several flare candidates in stars that are members of M67 and Rup 147. However, all but the events that occurred for four stars were false positives (SSOs), or the stars were not single members. Flare candidates in these old clusters appeared on RS CVn binaries, cataclysmic binaries, Algol type binaries, spectroscopic and eclipsing binaries, and red giant stars. Excluding these, we were left with one flare in M67 on a K1 dwarf. In Rup 147, we narrowed down the list to a flare on a G8 star in Rup 147, and four flares each on a K0.5 and an M3 star. For these stars, the multiplicity status is unknown. We found that the mass range of these stars as calculated from the uncertainties on the radii (?) is large enough that the stars could in principle be binary stars with undetected mid-M dwarf companions.

4.3. Flaring Activity Indicators

Flaring luminosity FA The energy released in flares was inferred using our derived stellar luminosities. It declines with T_{eff} for every T_{eff} bin considered for both the total luminosity relative to the quiescent flux (Fig. ??).

$L_{Kp,flare}$ is the luminosity in flares in the Kepler band. We can relate this to the quiescent bolometric luminosity of the star when we define the fractional flare luminosity FA in analogy to Paper

$$FA = \frac{E_{Kp,flare,tot}}{t \cdot L_{bol,*}}$$

We determined $L_{bol,*}$ from R_* and T_{eff} , as described in Sec. 2.4. In Fig. 8 we computed the median and standard deviation FA for every T_{eff} bin. FA is a meaningful measure of relative stellar activity as long as the flux portion of the quiescent star in the Kepler band is roughly constant. It is therefore more meaningful to compare FA values across age than across T_{eff} .

FFD Power law fit parameters to the FFDs (Figs. ?? and ??) are sensitive to the low-energy cutoff, where most observations

reside. The goodness of fit strongly depends on the sample size. Power law fit parameters derived using MLEs, as described in Sec. 3.3, are mostly consistent with each other but often deviate from $\alpha = 2$. A smaller sample size tends to create a flatter distribution (Figs. 9 and ??). Truncation was not detected for FFDs with more than 50 flares (Tables ?? and ??). For these results, extrapolations outside of the observed energy range are clearly off. If we assume $\alpha \equiv 2$, different distributions can be compared. For fixed α , in the ED domain, β_2 is the flare frequency at $ED = 1$ s, and shows a trend in both T_{eff} , and age (see Fig. ??). In the energy domain, the picture is less clear (Fig. ??).

Compare to other FFD values, e.g., from Ward's Evryscope survey, see table in Appendix, and maybe convert it to a plot Howard et al (2019) monitored superflares on cool stars with bolometric energies above 10^{33} erg and up to 10^{36} erg. They find power law exponent values around ~ 2 resolved by spectral types. Similar values are found for individual flare stars (Lurie et al. 2015). Howard+18, Loyd+18, Tilley+19 show that flares can erode exoplanetary atmospheres. If a flare is assumed to deposit its UV energy in an instant a single superflare can completely remove the ozone layer at the substellar point Loyd+18. Associated protons are safer way to ozone destruction if they are associated with reoccurring large flares Tilley+19

5. Discussion

5.1. Consistency with other studies

EvryFlare, mass-dependence,

5.2. Flaring and rotation

More energetic flares can be expected from faster rotating stars (Candelaresi et al. 2014; Doorselaere et al. 2017; Yang et al. 2017). Findings that flares with intermediate Rossby number appear to flare more than fast and slow rotators (Mondrik et al. 2019) could not be reproduced here or in the EvryFlare survey (Howard et al. 2019b). If enhanced flaring can be interpreted as an increase in the stellar angular momentum loss rate flaring activity can be used to inform the cause of variation in the spin-down efficiency. An example of such variations is the apparent temporary stalling of spin-down seen in K dwarfs in NGC 6811 (Curtis+2019). The authors favored a scenario in which the stellar core transfers momentum onto the envelope but did not rule out the possibility of a decreased magnetic braking efficiency. In the latter scenario, these stars should flare less.

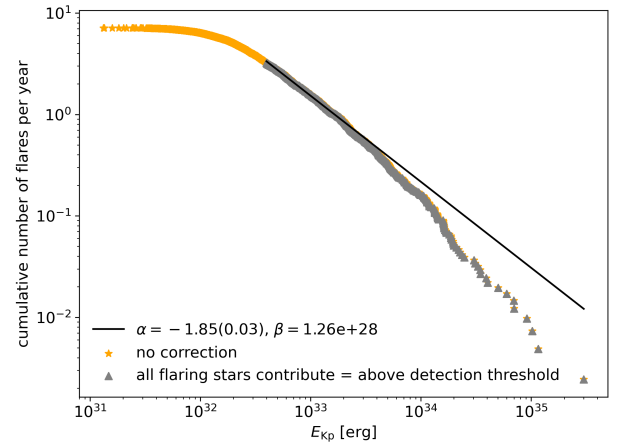
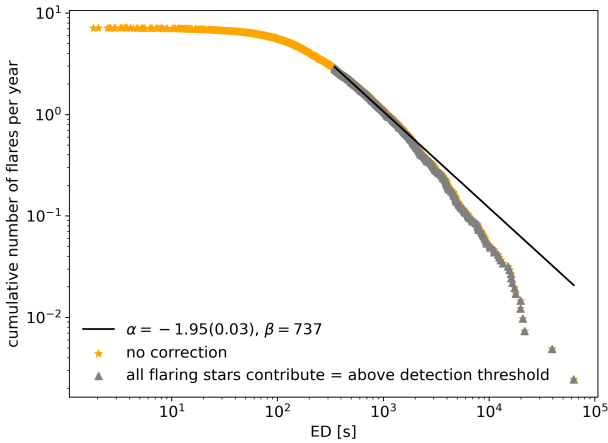
We used rotation periods derived from K2 light curves for the Pleiades (Rebull et al. 2016b), the Hyades (Douglas et al. 2016), and Praesepe (Rebull et al. 2017), to illuminate the rotation-flaring relation at fixed ages. In the Pleiades, most flaring stars are found on the fast rotator branch at or below one day, and flaring activity peaks in this regime. For Praesepe, flaring rates appear to [...] In the Hyades, all of the 11 stars with rotation periods that overlapped with our sample were found flaring, but the number were too low to provide statistical insight. For Rup 147, M35 and M67, no rotation rates were available at the time.

5.3. M37

Comparing our results to a similar study of photometric flares in M37 (Chang et al. 2015) we find the results somewhat discrepant. M37 is 300–600 Myr old and appears less active than Praesepe and Hyades in individual T_{eff} bins, which are of coeval

Table 2. Selection of confirmed flare candidates detected in open clusters observed by Kepler/K2, sorted by amplitude a . The full table is available on CDS.

| EPIC | C | cluster | c_0 | c_1 | a | T_{eff} [K] | ED [s] | $L_{\text{bol},*}$ [erg/s] | L_{Kp} [erg/s] |
|-----------|----|----------|--------|--------|-----------|----------------------|------------|----------------------------|-------------------------|
| 211079830 | 4 | Pleiades | 105984 | 105993 | 15.330194 | 3097(87) | 63340(63) | $8.29(3.34)10^{29}$ | $3.32(1.34)10^{29}$ |
| 210720772 | 4 | Pleiades | 107181 | 107184 | 9.674757 | 3104(86) | 19901(7) | $8.66(3.45)10^{29}$ | $3.48(1.38)10^{29}$ |
| 247523445 | 13 | Hyades | 143106 | 143109 | 8.260956 | 2964(49) | 16615(11) | $4.33(1.09)10^{29}$ | $1.69(0.43)10^{29}$ |
| 212021131 | 5 | Praesepe | 108974 | 108980 | 7.421916 | 3215(68) | 19828(175) | $2.01(0.65)10^{30}$ | $8.22(2.65)10^{29}$ |
| 210978953 | 4 | Pleiades | 106762 | 106770 | 6.769888 | 3050(95) | 39467(125) | $6.20(2.63)10^{29}$ | $2.46(1.04)10^{29}$ |
| 211913613 | 16 | Praesepe | 156845 | 156849 | 6.690356 | 3218(66) | 21632(147) | $2.05(0.65)10^{30}$ | $8.37(2.63)10^{29}$ |
| 211127297 | 4 | Pleiades | 106754 | 106759 | 6.449569 | 3147(86) | 20830(5) | $1.13(0.45)10^{30}$ | $4.59(1.81)10^{29}$ |
| 211681193 | 5 | Praesepe | 108116 | 108120 | 5.570804 | 3182(76) | 11198(95) | $1.64(0.58)10^{30}$ | $6.68(2.37)10^{29}$ |
| 211024798 | 4 | Pleiades | 104822 | 104826 | 5.394897 | 3290(62) | 12524(63) | $2.58(0.75)10^{30}$ | $1.06(0.31)10^{30}$ |
| 211134185 | 4 | Pleiades | 103891 | 103896 | 4.951629 | 3127(96) | 17459(33) | $9.99(4.33)10^{29}$ | $4.03(1.75)10^{29}$ |
| 211095280 | 4 | Pleiades | 106283 | 106287 | 4.796979 | 3138(93) | 12186(10) | $1.06(0.45)10^{30}$ | $4.32(1.82)10^{29}$ |
| 211022535 | 4 | Pleiades | 104262 | 104267 | 3.994973 | 2953(76) | 15164(57) | $3.50(1.10)10^{29}$ | $1.37(0.43)10^{29}$ |
| 211010517 | 4 | Pleiades | 106680 | 106685 | 3.968907 | 3252(70) | 16241(171) | $2.09(0.68)10^{30}$ | $8.59(2.77)10^{29}$ |
| 210846442 | 4 | Pleiades | 104410 | 104415 | 3.959977 | 3311(79) | 13515(10) | $2.88(0.96)10^{30}$ | $1.18(0.40)10^{30}$ |
| 212017838 | 5 | Praesepe | 111183 | 111192 | 3.671037 | 3307(89) | 10274(10) | $3.35(1.22)10^{30}$ | $1.38(0.50)10^{30}$ |
| 211984058 | 5 | Praesepe | 109952 | 109965 | 3.320636 | 3124(97) | 16063(149) | $1.17(0.51)10^{30}$ | $4.73(2.06)10^{29}$ |
| 211912899 | 5 | Praesepe | 110700 | 110706 | 3.257997 | 3133(81) | 7967(16) | $1.24(0.47)10^{30}$ | $5.01(1.89)10^{29}$ |
| 211151674 | 4 | Pleiades | 106457 | 106467 | 3.166323 | 3072(93) | 17843(106) | $7.10(2.99)10^{29}$ | $2.84(1.19)10^{29}$ |
| 211822895 | 5 | Praesepe | 107809 | 107812 | 3.164494 | 3005(177) | 6883(31) | $5.68(3.98)10^{29}$ | $2.25(1.57)10^{29}$ |
| 211760567 | 5 | Praesepe | 109962 | 109965 | 3.061417 | 3245(58) | 7838(9) | $2.39(0.69)10^{30}$ | $9.84(2.83)10^{29}$ |
| 211939350 | 16 | Praesepe | 155018 | 155022 | 2.892939 | 3149(150) | 9542(68) | $1.36(0.86)10^{30}$ | $5.52(3.49)10^{29}$ |
| 211137806 | 4 | Hyades | 106768 | 106775 | 2.482828 | 3127(58) | 9208(8) | $1.16(0.35)10^{30}$ | $4.69(1.40)10^{29}$ |
| 210674207 | 13 | Hyades | 141708 | 141711 | 2.419586 | 3210(74) | 5343(3) | $1.90(0.65)10^{30}$ | $7.78(2.66)10^{29}$ |
| 211994910 | 5 | Praesepe | 109858 | 109864 | 2.401426 | 3325(95) | 7807(14) | $3.71(1.40)10^{30}$ | $1.53(0.58)10^{30}$ |
| 211010517 | 4 | Pleiades | 106561 | 106564 | 2.341076 | 3252(70) | 4838(36) | $2.09(0.68)10^{30}$ | $8.59(2.77)10^{29}$ |
| 211984058 | 5 | Praesepe | 108584 | 108587 | 2.155468 | 3124(97) | 4817(13) | $1.17(0.51)10^{30}$ | $4.73(2.06)10^{29}$ |
| 211983544 | 18 | Praesepe | 162792 | 162798 | 2.096077 | 3159(98) | 6924(55) | $1.44(0.63)10^{30}$ | $5.88(2.55)10^{29}$ |
| 210988354 | 4 | Pleiades | 106012 | 106017 | 2.057812 | 3661(144) | 5725(1) | $1.40(0.31)10^{31}$ | $6.06(1.32)10^{30}$ |
| 210886447 | 4 | Pleiades | 103871 | 103877 | 2.057490 | 3048(105) | 8710(49) | $6.13(2.83)10^{29}$ | $2.43(1.12)10^{29}$ |
| 211098921 | 4 | Pleiades | 105254 | 105262 | 2.041041 | 3300(101) | 7499(5) | $2.72(1.10)10^{30}$ | $1.12(0.45)10^{30}$ |

**Fig. 5.** FFD (scatter) in ED (left panel) and energy (right panel) and respective power law fit (black line) to the full sample of flare candidates.**Table 3.** Mass budget of flaring stars in M67 and Rup 147 within 0.38 or older. We attribute the difference to the loose membership requirement of $pmem \geq 0.2$ in Chang et al. (2015) as compared to our stricter cuts at 0.8. We expect the M37 to be contaminated with field stars that systematically reduce the flaring rates. Applying our own restriction the M37 sample (Chang et al. 2016) leaves very few flares that hamper a statistical description of their distributions.

| EPIC | median SpT | binary |
|-----------|------------|-------------|
| 211434440 | K1 | K2 + M5.5 |
| 219601739 | G8 | K1 + M6 |
| 219610232 | K0.5 | K2 + M5.5 |
| 219591752 | M3 | M3.5 + M3.5 |

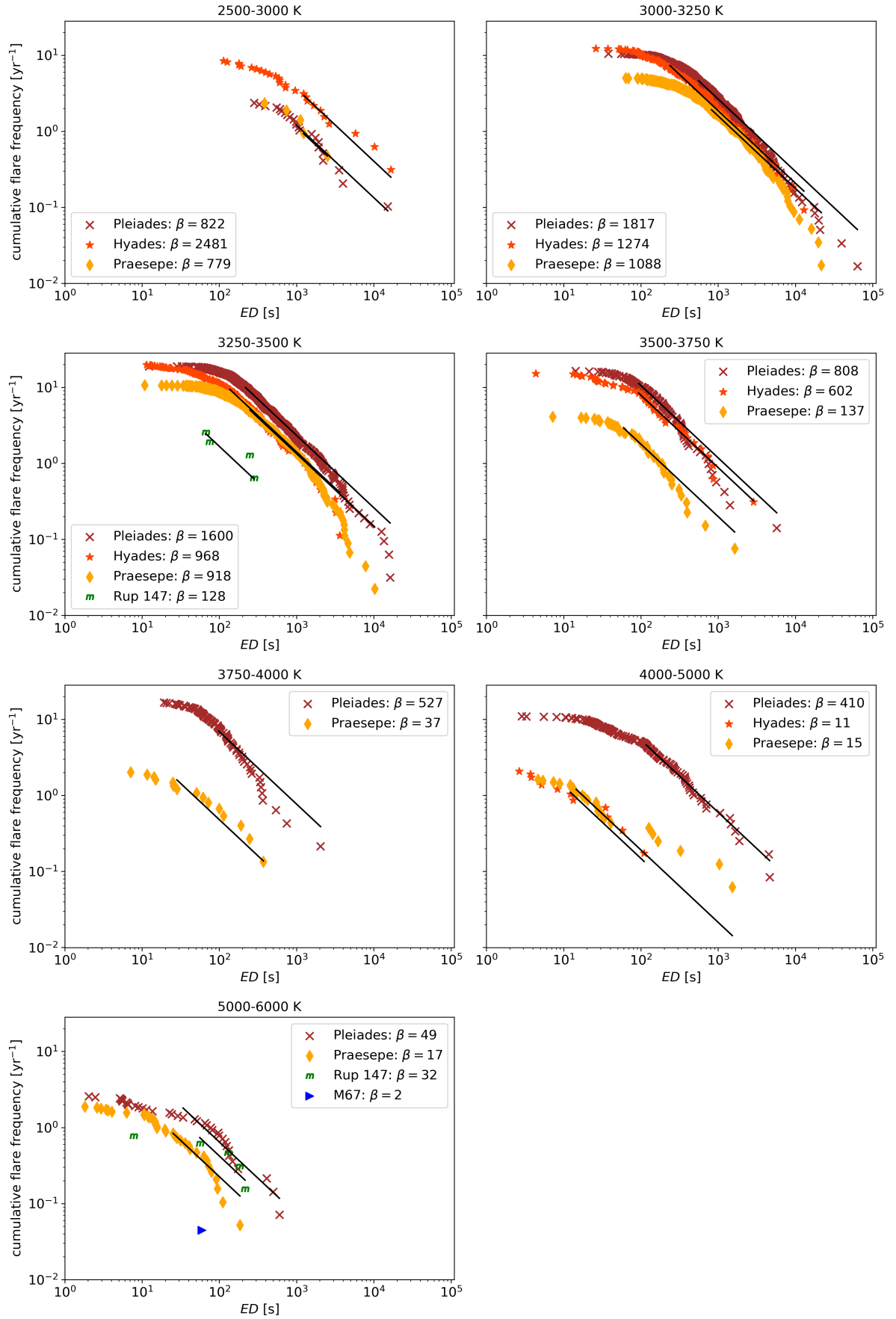


Fig. 6. FFDs (scatter) in ED and respective power law fits with $\alpha = \beta$ (black lines).

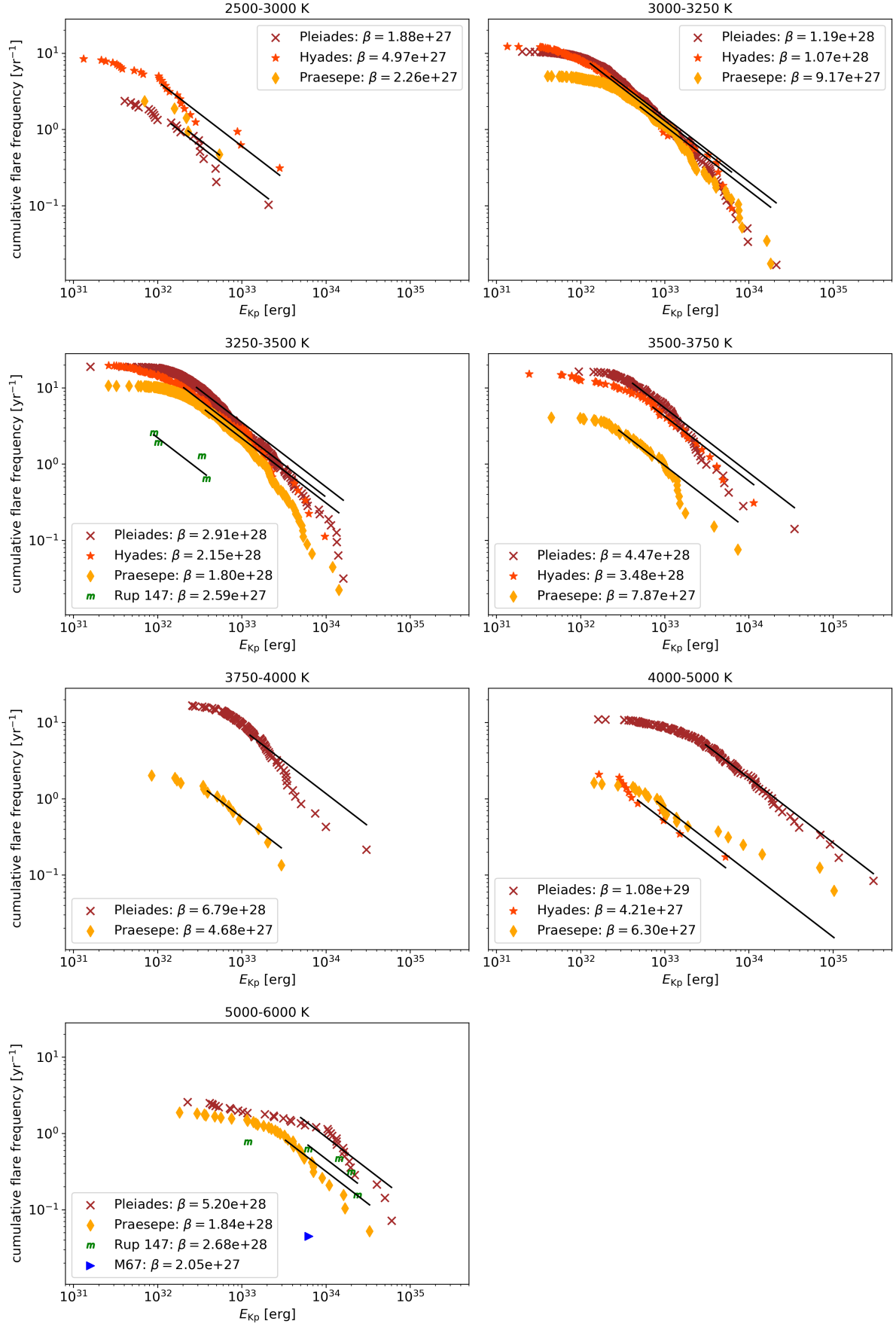


Fig. 7. FFDs (scatter) in energy and respective power law fits with $\alpha = \text{XXX}$ (black lines).

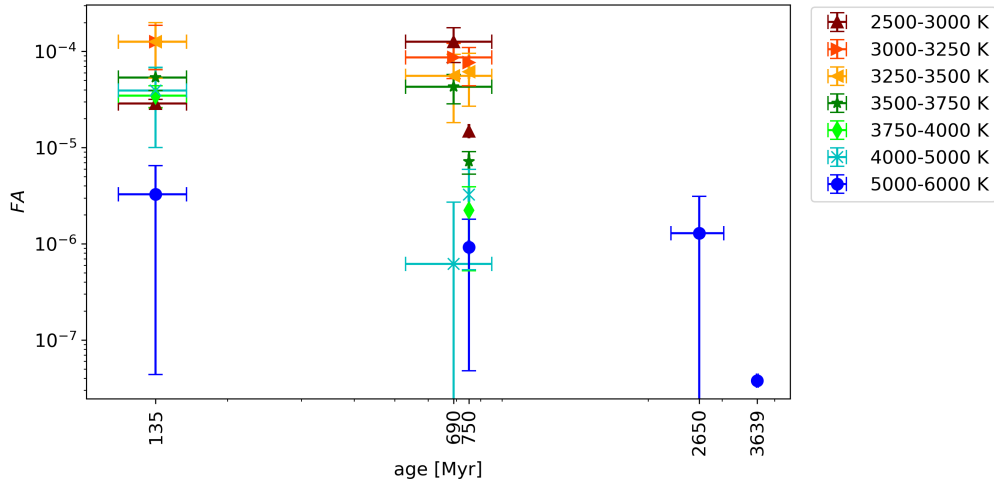


Fig. 8. *FA* for flares above the shared energy threshold as determined for the full FFD in Fig. 5.

Table 4. Summary of flaring β of all clusters and T_{eff} bins in E_{Kp} and ED distributions.

| | | β_s | n_s | tr_s | pl_s | β_{erg} | n_{erg} | tr_{erg} | pl_{erg} |
|-----------|----------|----------------------------|-------|--------|--------|-----------------------------------|------------------|-------------------|-------------------|
| 2500-3000 | Hyades | $2.48 (0.1) \cdot 10^3$ | 27 | False | True | $0.65 (0.02) \cdot 10^{28}$ | 27 | False | True |
| | Pleiades | $0.82 (0.03) \cdot 10^3$ | 23 | False | True | $2.46 (0.09) \cdot 10^{27}$ | 23 | False | True |
| | Praesepe | $0.777 (0.024) \cdot 10^3$ | 5 | False | True | $2.968 (0.093) \cdot 10^{27}$ | 5 | False | True |
| 3000-3250 | Hyades | $1.27 (0.04) \cdot 10^3$ | 133 | False | True | $1.401 (0.038) \cdot 10^{28}$ | 133 | False | True |
| | Pleiades | $1.814 (0.055) \cdot 10^3$ | 623 | False | True | $1.559 (0.042) \cdot 10^{28}$ | 623 | True | True |
| | Praesepe | $1.086 (0.033) \cdot 10^3$ | 289 | True | True | $1.205 (0.033) \cdot 10^{28}$ | 289 | True | True |
| 3250-3500 | Hyades | $0.966 (0.03) \cdot 10^3$ | 175 | False | True | $2.812 (0.076) \cdot 10^{28}$ | 175 | False | True |
| | Pleiades | $1.597 (0.049) \cdot 10^3$ | 598 | True | True | $0.382 (0.01) \cdot 10^{29}$ | 598 | True | True |
| | Praesepe | $0.917 (0.028) \cdot 10^3$ | 477 | True | True | $2.36 (0.064) \cdot 10^{28}$ | 477 | True | False |
| | Rup 147 | $1.28 (0.12) \cdot 10^2$ | 4 | False | True | $0.34 (0.03) \cdot 10^{28}$ | 4 | False | True |
| 3500-3750 | Hyades | $0.6 (0.02) \cdot 10^3$ | 49 | False | True | $0.458 (0.014) \cdot 10^{29}$ | 49 | False | True |
| | Pleiades | $0.807 (0.025) \cdot 10^3$ | 116 | False | True | $0.588 (0.016) \cdot 10^{29}$ | 116 | False | True |
| | Praesepe | $1.36 (0.05) \cdot 10^2$ | 54 | False | True | $1.032 (0.031) \cdot 10^{28}$ | 54 | False | True |
| 3750-4000 | Pleiades | $0.53 (0.02) \cdot 10^3$ | 78 | False | True | $0.89 (0.03) \cdot 10^{29}$ | 78 | False | False |
| | Praesepe | $0.37 (0.08) \cdot 10^2$ | 15 | False | True | $0.61 (0.02) \cdot 10^{28}$ | 15 | False | True |
| 4000-5000 | Hyades | $1.13 (0.11) \cdot 10^1$ | 12 | False | True | $0.55 (0.06) \cdot 10^{28}$ | 12 | False | True |
| | Pleiades | $0.41 (0.013) \cdot 10^3$ | 131 | False | True | $1.434 (0.039) \cdot 10^{29}$ | 131 | False | True |
| | Praesepe | $1.46 (0.07) \cdot 10^1$ | 26 | False | True | $0.83 (0.03) \cdot 10^{28}$ | 26 | False | True |
| 5000-6000 | M67 | $2.19 (0.31) \cdot 10^0$ | 1 | True | False | $2.70328 (0.00027) \cdot 10^{27}$ | 1 | True | False |
| | Pleiades | $0.49 (0.05) \cdot 10^2$ | 36 | False | True | $0.69 (0.04) \cdot 10^{29}$ | 36 | False | True |
| | Praesepe | $1.73 (0.06) \cdot 10^1$ | 36 | False | True | $2.44 (0.09) \cdot 10^{28}$ | 36 | False | True |
| | Rup 147 | $0.32 (0.08) \cdot 10^2$ | 5 | False | True | $0.36 (0.05) \cdot 10^{29}$ | 5 | False | True |

Table 5. Summary of FFD parameters and power law fits to the full sample of all clusters in E_{Kp} and ED space.

| | ED | E_{Kp} |
|------------------------------|------------|---------------------|
| α | 1.95(0.03) | 1.85(0.03) |
| β [yr^{-1}] | 785(24) | $1.75(0.05)10^{28}$ |
| n_{tot} | 2913 | 2913 |
| n_{fit} | 1166 | 1336 |
| tr | True | True |
| pl | False | False |

5.4. Division at 3000 K

The lowest T_{eff} bin at Pleiades age in our sample reflects the division between fully convective stars and those with a radiative core (Reid & Hawley 2005). At this age, the coolest dwarfs

may still be accreting angular momentum on the PMS, instead of spinning down on the MS. We suggest that a regime change occurs around 120 Myr for stars with $T_{\text{eff}} = 2500 - 3250$ K. Below 3000 K, an analysis of 66 ZDI maps show that magnetic field configurations can be strong and dipolar or weak and multipolar (Morin et al. 2008; See et al. 2017). If these stars can be distinguished by age, this should be reflected in our age-resolved flaring activity. If the difference is not a function of age, we should see a similar bimodal distribution of very inactive and very active stars in the lowest mass bins. If the difference between the two configurations is a function of age, we should only see one type of stars with correspondingly similar behaviour in these T_{eff} bins.

The lowest mass bin appears underactive compared to the rest of the flaring-age- T_{eff} relation in the ED domain. Physical explanations for this peculiarity include: A different magnetic structure

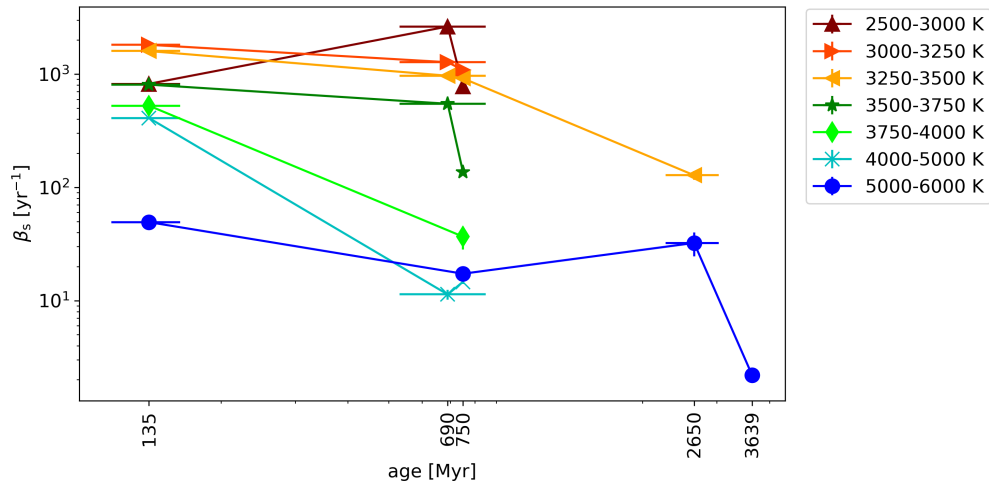


Fig. 9. Flare β_s vs. age grouped by T_{eff} .

A truncation of the power law that reflects the maximum ED_{max} active region can produce on these stars. West et al. (2015) found that all M1-M4 dwarfs with rotation periods shorter than 26 days, and all M5-M8 dwarfs with periods shorter than 86 days show $H\alpha$ emission, indicating their magnetic activity. Assuming a typical binary fraction for early and mid dwarfs (Fischer & Marcy 1992), we can expect some of the flares on stars at $T_{\text{eff}} > 3000$ K to belong to unresolved binary companions with $T_{\text{eff}} < 3000$ K. A misattributed flare on an early dwarf then will be assigned a too small ED , but still a correct $E_{\text{Kp,flare}}$ because the count ratios are equal to the L_{Kp} ratios.

5.5. Consistency of Hyades' and Praesepe's results

HRDs constructed in Gaia Collaboration et al. (2018a) indicate only slightly older ages for Hyades and Praesepe. We expect our results to reflect this similarity. *Are the samples comparable? Membership determination may differ. Can we frame this as a statistical test, i.e. answer the question: What is the probability that the activity distributions for both clusters were drawn from the same underlying distribution for a given age and mass bin?* Metallicity is controlled for ($[\text{Fe}/\text{H}](\text{Praesepe}) = 0.16$, $[\text{Fe}/\text{H}](\text{Hyades}) = 0.13$, Netopil et al. 2016).

5.6. Consistency of Pleiades and M35 results

M35 is has subsolar metallicity, while Pleiades are roughly solar.

5.7. Jim's section(s)

Flaring activity function of mass and age – a gyrochronology analog? Results in the context of Davenport et al. (2019): How well does the model fit if we have isochronal and not rotational ages for our stars? Davenport et al. (2019) note a sample bias towards more active stars. Their models overpredicts the superflaring rate of the average Sun-like sample from Shibayama et al. (2013) and more resembles the rate for their most active sub-sample. *Do we see the same effect in our OC sample? We should not. Or cluster memberships depend on activity.*

5.8. Universality of α

Taken into account uncertainties and systematic errors resulting from power law fitting methods, the power law exponent $\alpha \sim 2$ appears to be the same for all studies on flare statistics so far, irrespective of spectral type. A notable exception are A stars in Kepler that follow a power law with $\alpha \sim 1$ that may indicate a different physical process (Yang & Liu 2019).

5.9. Deviations from single power law

Spots can survive on the stellar surface from a few days to nearly a year (Namekata et al. 2017; Davenport 2015). Namekata et al. (2017) find conceivable that spots evolve on timescale shorter than the estimated lifetimes. Complex spot geometry is correlated with the strongest X-class flares on the Sun (Toriumi et al. 2017; Sammis et al. 2000). This supports the idea that flares are associated with the presence of certain types of starspots, or more generally, certain types of active regions. Since we can reasonably expect that there is a maximum flare energy a spot can produce, the underlying power law relation must break at some ED_{max} . We tested a possible truncation of our FFDs, but find no conclusive evidence for it in any FFD with > 50 data points. As we stack multiple targets, each potentially with multiple, evolving spots of various sizes on their surfaces, into one FFD at a time, we might observe a deviation but no truncation. A different explanation is simply that we do not sample the maximum energies, as extremely high relative fluxes have been observed in the past (Paudel et al. 2018; Jackman et al. 2019; Schmidt et al. 2016).

6. Summary and Conclusions

Is there or will be there more data available to further extend the sample? There are no model-independent stellar ages. It is more correct to speak of evolutionary stage. Stars in open clusters with precise isochronal ages have their observables reduced to a number of years. We can now ask: Can we unambiguously map flaring evolutionary stage to the evolutionary stage of isochronal fit parameters of a given star? If there is either a strong correlation, or even a physical relation between flaring activity and, for instance, mass and rotation rate, the answer is yes. If this relation is sufficiently sensitive to be captured by present day instrumen-

tation, and non-degenerate in the relevant parameters, flaring activity can be integrated into the family of age indicators, and complement and extend them. Ultimately, flaring activity depends on how efficiently the star converts its energy budget to flares throughout its lifetime. Since the fraction of total luminosity released in flares is small even for the most active stars, this efficiency need not scale directly with the overall energy budget of the star on the MS, but will more likely depend on the ability of the star to use this budget to produce magnetic surface topologies and strengths that enable flaring. A magnetic dynamo, driven by rotation and convection, introduces magnetic field to the system that causes stellar wind that in turn removes angular momentum from the star, decreasing rotation rate. Over time, the wind takes away more and more angular momentum, and the global magnetic field weakens. This is reflected in observations of chromospheric indicators (ZDI??). The decline is famously known as the Skumanich law, and gave rise to the rotational age-dating technique called gyrochronology. However, recent studies noted deviations from this rule, stalling of the spin-down, and offered multiple competing explanations. It is not clear how these effects reflect on the small-scale surface magnetic field. Chromospheric activity on solar-type stars seems to continue to decline regardless of these rotational effects. What about X-ray? Observationally, not much can be directly said about the small-scale topology of stellar magnetic fields beyond extrapolations from the solar case. On the Sun, chromospheric activity indicates line emission in excess of radiative equilibrium that is caused by magnetic fields. Likewise, magnetic field effects heat the corona.

Acknowledgements. This work made use of the *gaia-kepler.fun* crossmatch database created by Megan Bedell. Kepler-affiliated tools were used in the process: *lightkurve*, *K2SC*, *AltaiPony*. Also: *numpy*, *pandas*, *astroML*, *astrometry*, *specmatch-emp*, *bokeh* (Bokeh Development Team 2019)... TOPCAT: This research made use of the cross-match service provided by CDS, Strasbourg. This work has made use of data from the European Space Agency (ESA) mission *Gaia* (<https://www.cosmos.esa.int/gaia>), processed by the *Gaia* Data Processing and Analysis Consortium (DPAC, <https://www.cosmos.esa.int/web/gaia/dpac/consortium>). Funding for the DPAC has been provided by national institutions, in particular the institutions participating in the *Gaia* Multilateral Agreement. If you have used *Gaia* DR2 data in your research, please cite both the *Gaia* mission paper and the *Gaia* DR2 release paper: *Gaia Collaboration et al.* (2016): Description of the *Gaia* mission (spacecraft, instruments, survey and measurement principles, and operations), *Gaia Collaboration et al.* (2018b): Summary of the contents and survey properties.

References

Aarnio, A. N., Matt, S. P., & Stassun, K. G. 2012, *ApJ*, 760, 9
Aarnio, A. N., Stassun, K. G., Hughes, W. J., & McGregor, S. L. 2011, *Sol. Phys.*, 268, 195
Aigrain, S., Parviainen, H., & Pope, B. J. S. 2016, *MNRAS*, 459, 2408
Alvarado-Gómez, J. D., Drake, J. J., Cohen, O., Moschou, S. P., & Garraffo, R. M. 2018, *ApJ*, 862, 93
Anders, F., Khalatyan, A., Chiappini, C., et al. 2019, *A&A*, 628, A94
Andrae, R., Fouesneau, M., Creevey, O., et al. 2018, *A&A*, 616, A8
Bailer-Jones, C. A. L., Andrae, R., Arcay, B., et al. 2013, *A&A*, 559, A74
Barentsen, G., Hedges, C., Saunders, N., et al. 2018, *arXiv e-prints*, arXiv:1810.12554
Barnes, S. A. 2003, *ApJ*, 586, 464
Bauke, H. 2007, *European Physical Journal B*, 58, 167
Bessell, M. S. & Brett, J. M. 1988, *Publications of the Astronomical Society of the Pacific*, 100, 1134
Bochanski, J. J., Hawley, S. L., Covey, K. R., et al. 2010, *AJ*, 139, 2679
Bochanski, J. J., West, A. A., Hawley, S. L., & Covey, K. R. 2007, *AJ*, 133, 2384
Bokeh Development Team. 2019, *Bokeh: Python library for interactive visualization*
Bouy, H., Bertin, E., Barrado, D., et al. 2015, *Astronomy and Astrophysics*, A120

Boyajian, T. S., von Braun, K., van Belle, G., et al. 2013, *The Astrophysical Journal*, 771, 40
Burgasser, A. J., Cruz, K. L., Cushing, M., et al. 2010, *ApJ*, 710, 1142
Burgasser, A. J., Liu, M. C., Ireland, M. J., Cruz, K. L., & Dupuy, T. J. 2008, *ApJ*, 681, 579
Burgasser, A. J., Looper, D. L., Kirkpatrick, J. D., & Liu, M. C. 2007, *ApJ*, 658, 557
Burgasser, A. J. & McElwain, M. W. 2006, *AJ*, 131, 1007
Burgasser, A. J., McElwain, M. W., Kirkpatrick, J. D., et al. 2004, *AJ*, 127, 2856
Candelaresi, S., Hillier, A., Maehara, H., Brandenburg, A., & Shibata, K. 2014, *ApJ*, 792, 67
Cantat-Gaudin, T., Jordi, C., Vallenari, A., et al. 2018, *A&A*, 618, A93
Carpenter, J. M. 2001, *The Astronomical Journal*, 121, 2851
Chambers, K. C., Magnier, E. A., Metcalfe, N., et al. 2016, *ArXiv e-prints* [arXiv:1612.05560]
Chang, S.-W., Byun, Y.-I., & Hartman, J. D. 2015, *ApJ*, 814, 35
Chang, S. W., Byun, Y. I., & Hartman, J. D. 2016, *VizieR Online Data Catalog*, J/ApJ/814/35
Clarke, R. W., Davenport, J. R. A., Covey, K. R., & Baranec, C. 2018, *ApJ*, 853, 59
Cruz, K. L., Burgasser, A. J., Reid, I. N., & Liebert, J. 2004, *ApJ*, 604, L61
Cruz, K. L., Reid, I. N., Liebert, J., Kirkpatrick, J. D., & Lowrance, P. J. 2003, *AJ*, 126, 2421
Curtis, J. L., Wolfgang, A., Wright, J. T., Brewer, J. M., & Johnson, J. A. 2013, *AJ*, 145, 134
Davenport, J. 2015, PhD thesis, University of Washington
Davenport, J. R. A., Covey, K. R., Clarke, R. W., et al. 2019, *ApJ*, 871, 241
Davenport, J. R. A., Hawley, S. L., Hebb, L., et al. 2014, *ApJ*, 797, 122
Doi, M., Tanaka, M., Fukugita, M., et al. 2010, *AJ*, 139, 1628
Doorselaere, T. V., Shariati, H., & Debosscher, J. 2017, *ApJS*, 232, 26
Douglas, S. T., Agüeros, M. A., Covey, K. R., et al. 2014, *ApJ*, 795, 161
Douglas, S. T., Agüeros, M. A., Covey, K. R., et al. 2016, *ApJ*, 822, 47
Douglas, S. T., Agüeros, M. A., Covey, K. R., & Kraus, A. 2017, *ApJ*, 842, 83
Drake, J. J., Cohen, O., Yashiro, S., & Gopalswamy, N. 2013, *ApJ*, 764, 170
Filippazzo, J. C., Rice, E. L., Faherty, J., et al. 2015, *ApJ*, 810, 158
Finkbeiner, D. P., Schlafly, E. F., Schlegel, D. J., et al. 2016, *ApJ*, 822, 66
Fischer, D. A. & Marcy, G. W. 1992, *ApJ*, 396, 178
Froning, C. S., Kowalski, A., France, K., et al. 2019, *ApJ*, 871, L26
Gaia Collaboration, Babusiaux, C., van Leeuwen, F., et al. 2018a, *A&A*, 616, A10
Gaia Collaboration, Brown, A. G. A., Vallenari, A., et al. 2018b, *A&A*, 616, A1
Gao, X. 2018, *ApJ*, 869, 9
Gao, X. 2018, *The Astrophysical Journal*, 869, 9
Gizis, J. E. 2013, *ApJ*, 779, 172
Gonzalez, G. 2016, *MNRAS*, 459, 1060
Green, G. M., Schlafly, E. F., Finkbeiner, D., et al. 2018, *MNRAS*, 478, 651
Green, G. M., Schlafly, E. F., Zucker, C., Speagle, J. S., & Finkbeiner, D. P. 2019, *arXiv e-prints*, arXiv:1905.02734
Hawley, S. L. & Fisher, G. H. 1992, *ApJS*, 78, 565
Hilton, E. J., West, A. A., Hawley, S. L., & Kowalski, A. F. 2010, *AJ*, 140, 1402
Howard, W. S., Corbett, H., Law, N. M., et al. 2019a, *ApJ*, 881, 9
Howard, W. S., Corbett, H., Law, N. M., et al. 2019b, *arXiv e-prints*, arXiv:1907.10735
Howell, S. B., Sobeck, C., Haas, M., et al. 2014, *PASP*, 126, 398
Hunt-Walker, N. M., Hilton, E. J., Kowalski, A. F., Hawley, S. L., & Matthews, J. M. 2012, *PASP*, 124, 545
Ilin, E., Schmidt, S. J., Davenport, J. R. A., & Strassmeier, K. G. 2019, *A&A*, 622, A133
Jackman, J. A. G., Wheatley, P. J., Bayliss, D., et al. 2019, *arXiv e-prints*, arXiv:1902.00900
Karoff, C. 2016, *Nature Communications*, 7, 11058
Kerr, G. S. & Fletcher, L. 2014, *ApJ*, 783, 98
Kirkpatrick, J. D., Looper, D. L., Burgasser, A. J., et al. 2010, *ApJS*, 190, 100
Kleint, L., Heinzel, P., Judge, P., & Krucker, S. 2016, *ApJ*, 816, 88
Koch, D. G., Borucki, W. J., Basri, G., et al. 2010, *ApJ*, 713, L79
Kovács, G., Bakos, G., & Noyes, R. W. 2005, *MNRAS*, 356, 557
Kowalski, A. F., Hawley, S. L., Wisniewski, J. P., et al. 2013, *ApJS*, 207, 15
Kretzschmar, M. 2011, *A&A*, 530, A84
Lecavelier des Etangs, A., Bourrier, V., Wheatley, P. J., et al. 2012, *A&A*, 543, L4
Lloyd, R. O. P., France, K., Youngblood, A., et al. 2018, *ApJ*, 867, 71
Luger, R., Kruse, E., Foreman-Mackey, D., Agol, E., & Saunders, N. 2018, *AJ*, 156, 99
Lurie, J. C., Davenport, J. R. A., Hawley, S. L., et al. 2015, *ApJ*, 800, 95
Mann, A. W., Feiden, G. A., Gaidos, E., Boyajian, T., & von Braun, K. 2015, *ApJ*, 804, 64
Mann, A. W., Feiden, G. A., Gaidos, E., Boyajian, T., & von Braun, K. 2016, *The Astrophysical Journal*, 819, 87
Maschberger, T. & Kroupa, P. 2009, *MNRAS*, 395, 931
Mondrik, N., Newton, E., Charbonneau, D., & Irwin, J. 2019, *ApJ*, 870, 10

788 Morin, J., Donati, J. F., Petit, P., et al. 2008, MNRAS, 390, 567
 789 Namekata, K., Sakaue, T., Watanabe, K., et al. 2017, ApJ, 851, 91
 790 Nardiello, D., Libralato, M., Bedin, L. R., et al. 2016, MNRAS, 463, 1831
 791 Olivares, J., Bouy, H., Sarro, L. M., et al. 2019, A&A, 625, A115
 792 Olivares, J., Sarro, L. M., Moraux, E., et al. 2018, A&A, 617, A15
 793 Paudel, R. R., Gizis, J. E., Mullan, D. J., et al. 2018, ApJ, 861, 76
 794 Pecaut, M. J. & Mamajek, E. E. 2013, ApJS, 208, 9
 795 Priest, E. & Forbes, T. 2002, A&A Rev., 10, 313
 796 Queiroz, A. B. A., Anders, F., Santiago, B. X., et al. 2018, MNRAS, 476, 2556
 797 Rayner, J. T., Cushing, M. C., & Vacca, W. D. 2009, ApJS, 185, 289
 798 Rebull, L., Stauffer, J., Bouvier, J., et al. 2016a, Astronom-
 799 ical Journal, 152, 113, bibtex: 2016AJ....152..113R bib-
 800 tex[eid=113;adsurl=https://ui.adsabs.harvard.edu/abs/2016AJ....152..113R;adsnote=Provided
 801 by the SAO/NASA Astrophysics Data System]
 802 Rebull, L. M., Stauffer, J. R., Bouvier, J., et al. 2016b, AJ, 152, 113
 803 Rebull, L. M., Stauffer, J. R., Hillenbrand, L. A., et al. 2017, ApJ, 839, 92
 804 Reid, I. N. & Hawley, S. L. 2005, New Light on Dark Stars: Red Dwarfs, Low-
 805 Mass Stars, Brown Dwarfs, 2nd edn., Springer-Praxis books in astronomy and
 806 astrophysics (Berlin ; New York : Chichester, UK: Springer ; Praxis)
 807 Reino, S., de Bruijne, J., Zari, E., d'Antona, F., & Ventura, P. 2018, MNRAS,
 808 477, 3197
 809 Sammis, I., Tang, F., & Zirin, H. 2000, ApJ, 540, 583
 810 Schmidt, S. J. 2014, Mem. Soc. Astron. Italiana, 85, 741
 811 Schmidt, S. J., Hawley, S. L., West, A. A., et al. 2015, AJ, 149, 158
 812 Schmidt, S. J., Shappee, B. J., Gagné, J., et al. 2016, ApJ, 828, L22
 813 Schmidt, S. J., West, A. A., Bochanski, J. J., Hawley, S. L., & Kietly, C. 2014,
 814 PASP, 126, 642
 815 Schmidt, S. J., West, A. A., Hawley, S. L., & Pineda, J. S. 2010, AJ, 139, 1808
 816 See, V., Jardine, M., Vidotto, A. A., et al. 2017, MNRAS, 466, 1542
 817 Shibayama, T., Maehara, H., Notsu, S., et al. 2013, The Astrophysical Journal
 818 Supplement Series, 209, 5
 819 Shibayama, T., Maehara, H., Notsu, S., et al. 2013, ApJS, 209, 5
 820 Skrutskie, M. F., Cutri, R. M., Stiening, R., et al. 2006, AJ, 131, 1163
 821 Soares-Furtado, M., Hartman, J. D., Bakos, G. Á., et al. 2017, Publications of
 822 the Astronomical Society of the Pacific, 129, 044501
 823 Tilley, M. A., Segura, A., Meadows, V., Hawley, S., & Davenport, J. 2019, As-
 824 trobiology, 19, 64
 825 Toriumi, S., Schrijver, C. J., Harra, L. K., Hudson, H., & Nagashima, K. 2017,
 826 ApJ, 834, 56
 827 Van Cleve, J. E., Howell, S. B., Smith, J. C., et al. 2016, PASP, 128, 075002
 828 Vanderburg, A. & Johnson, J. A. 2014, Publications of the Astronomical Society
 829 of the Pacific, 126, 948
 830 Vanderplas, J., Connolly, A., Ivezić, Ž., & Gray, A. 2012, in Conference on In-
 831 telligent Data Understanding (CIDU), 47 –54
 832 Vinícius, Z., Barentsen, G., Hedges, C., Gully-Santiago, M., & Cody, A. M. 2018
 833 Walkowicz, L. M., Basri, G., Batalha, N., et al. 2011, AJ, 141, 50
 834 Watanabe, K., Shimizu, T., Masuda, S., Ichimoto, K., & Ohno, M. 2013, ApJ,
 835 776, 123
 836 West, A. A., Morgan, D. P., Bochanski, J. J., et al. 2011, AJ, 141, 97
 837 West, A. A., Weisenburger, K. L., Irwin, J., et al. 2015, ApJ, 812, 3
 838 Wheatland, M. S. 2004, ApJ, 609, 1134
 839 Yang, H. & Liu, J. 2019, ApJS, 241, 29
 840 Yang, H., Liu, J., Gao, Q., et al. 2017, ApJ, 849, 36
 841 Yee, S. W., Petigura, E. A., & von Braun, K. 2017, ApJ, 836, 77

Appendix A: Membership probabilities

To match catalogs on RA and declination we used `astroML.crossmatch` tool for Python (Vanderplas et al. 2012). For the studies with classifiers we assigned membership probabilities as follows. In Gonzalez (2016):

$$\begin{aligned} p(M(\text{member})) &= 0.9, \\ p(BM(\text{binary member})) &= 0.9, \\ p(N(\text{non-member})) &= 0.1, \\ p(SN(\text{single non-member})) &= 0.1, \\ p(BN(\text{binary non-member})) &= 0.1, \\ p(U(\text{unknown member})) &= 0.5. \end{aligned}$$

In Curtis et al. (2013):

$$\begin{aligned} p(Y(\text{highest confidence member})) &= 0.9, \\ p(P(\text{possible/probable member})) &= 0.7, \\ p(N(\text{not likely/non-member})) &= 0.7, \\ p(B(\text{photometry consistent with blue stragglers})) &= 0.0. \end{aligned}$$

In Rebull et al. (2017):

$$\begin{aligned} p((\text{best})) &= 0.9, \\ p((\text{ok})) &= 0.6, \\ p((\text{else})) &= 0.1. \end{aligned}$$

Members from Rebull et al. (2016a); Douglas et al. (2017); and Gaia Collaboration et al. (2018a) were assigned $p = 0.9$ if they appeared in the final catalog. Table A.1 gives an overview over different membership catalogs. Figure A.1 shows membership probability histograms of the final sample broken down by membership source. Detailed instructions on how to reproduce the final sample of members in each cluster, and corresponding tables, Python scripts, and Jupyter notebooks can be found online⁵

Appendix B: Cluster parameters

Appendix C: Broadband photometry: quality cuts and conversions

We required `flux/flux_error` ≥ 10 for Gaia G, BP, and RP bands. We require that the 2MASS measurements for J, H, and K to be "A". "A" means that measurements had $S/N > 10$ and $\sigma < 0.11$. For PanSTARRS photometry, we required that the `QF_OBJ_GOOD` quality filter flag was set. SDSS and PS1 *ugrizy* bands are similar but not identical, but can be converted using Table 2 in Finkbeiner et al. (2016).

Appendix D: Pixel saturation

Resolve different levels of pixel saturation (>1 , >10) and how they contribute to the deviations from the single power law at the highest energies.

⁵ <https://github.com/ekaterinailin/flares-in-clusters-with-k2-ii>

Appendix E: Solar system objects

Solar system objects (SSOs) produce brightness excursions in K2 light curves that can closely resemble flare signatures. Often, they can be distinguished by their symmetric rise and decay shape as contrasted with the typical fast-rise gradual decay flare shape (Davenport et al. 2014). M. H. Christiansen and colleagues developed a routine called `SkyBoT` that matches positions and times to passages of SSOs listed in YYY. RA, declination, start, stop, and mid epochs of flares in BKJD are the input parameters. We excluded all flare candidates that occurred within X minutes of a SSO passage at the star's position. This procedure removed ZZ% of all flare candidates. In the case of high energy flares, we confirmed the passage by manually inspecting the pixel file with the `lightkurve.interact` function for `TargetPixelFiles`.

Appendix F: Universality of power law exponent α

We compiled an exhaustive (?) table of previous work where power laws were fitted to FFDs using different methods. Table F.1 lists the overview. While particular studies consistently find values above or below $\alpha \approx 2$, the comparison of different studies points towards unresolved systematic errors in all these studies.

Appendix G: Expanding the likelihood

The rate λ_2 of flares with energies larger than S_2 is given in Wheatland (2004) as

$$\lambda_2 = \lambda_1 \cdot \left(\frac{S_1}{S_2} \right)^{\alpha-1}. \quad (\text{G.1})$$

S_1 denotes the energy above which all flares are detected. λ_1 is the corresponding rate. α remains the power law exponent of the flare frequency distribution.

We are also given the posterior distribution for the rate λ_2 of flares above S_2 in Eq. (20) in Wheatland (2004):

$$P_2(\lambda_2) = \int_1^\infty d\alpha \int_0^\infty d\lambda_1 \delta \left(\lambda_2 - \lambda_1 \cdot \left(\frac{S_1}{S_2} \right)^{\alpha-1} \right) \cdot P_1(\lambda_1) \cdot P_\alpha(\alpha) \quad (\text{G.2})$$

As we have additional information in the form of uncertainties in our data $S = \{S_i, \lambda_i, \sigma_{S,i}\}$, we can expand Eq. G.2 with this knowledge. Assuming that the observed flare energies S_i with cumulative rates λ_i are distributed around the real flare energies $S_{0,i}$ with Gaussian uncertainties $\sigma_{S,i}$, we can define:

$$\begin{aligned} p(S_i | \lambda_1, \alpha, \sigma_{S,i}) &= \frac{1}{2\pi \sqrt{\sigma_{S,i}}} e^{-\frac{(S_i - S_{0,i})^2}{2\sigma_{S,i}^2}} \\ &= \frac{1}{2\pi \sqrt{\sigma_{S,i}}} e^{-\frac{\left(S_i - S_1 \left(\frac{\lambda_i}{\lambda_1} \right)^{-1/(\alpha-1)} \right)^2}{2\sigma_{S,i}^2}} \end{aligned} \quad (\text{G.3})$$

We assume in Eq. G.3 that uncertainties on λ_1 are negligible. Eq. G.2 then reads:

$$P_2(\lambda_2) = \int_1^\infty d\alpha \int_0^\infty d\lambda_1 \delta \left(\lambda_2 - \lambda_1 \cdot \left(\frac{S_1}{S_2} \right)^{\alpha-1} \right) \cdot P_1(\lambda_1) \cdot P_\alpha(\alpha) \cdot P_S(S | \lambda_1, \alpha, \sigma_S) \quad (\text{G.4})$$

Table A.1. Membership catalogs overview. No distance are given for Hyades we adopted individual distances for all members.

| source | type | clusters covered | notes |
|-----------------------------------|--------------|---|-----------------|
| Curtis et al. (2013) | classifier | Rup 147 | |
| Douglas et al. (2014) | probability | Hyades, Praesepe | meta study |
| Gonzalez (2016) | classifier | M67 | |
| Rebull et al. (2016a) | members list | Pleiades | meta study |
| Rebull et al. (2017) | classifier | Praesepe | meta study |
| Douglas et al. (2017) | members list | Praesepe | meta study |
| Gaia Collaboration et al. (2018a) | members list | Hyades, Rup 147, Pleiades, Praesepe | Gaia DR2, (1) |
| Cantat-Gaudin et al. (2018) | probability | Rup 147, Pleiades, Praesepe | Gaia DR2 |
| Gao (2018) | probability | M67 | Gaia DR2 |
| Reino et al. (2018) | probability | Hyades | Gaia DR1, (1) |
| Olivares et al. (2018) | probability | Pleiades | Gaia DR2, DANCe |
| Olivares et al. (2019) | probability | Rup 147 | Gaia DR2, DANCe |

Notes. DANCe: DANCe membership study project. (1) Positions for Hyades were propagated to epoch 2000 using Gaia proper motions.

with

$$P_S(S|\lambda_1, \alpha, \sigma_S) = C \prod_{i=1}^M p(S_i|\lambda_1, \alpha, \sigma_{S,i}). \quad (\text{G.5})$$

905 C absorbs the normalization, or evidence term.
 906 Following Wheatland (2004), we marginalize over λ_1 using the
 907 δ function in G.4 to obtain

$$P_2(\lambda_2) = \int_1^\infty d\alpha \cdot P_1\left(\lambda_2 \cdot \left(\frac{S_2}{S_1}\right)^{\alpha-1}\right) \cdot P_\alpha(\alpha) \cdot P_S\left(S|\lambda_2 \cdot \left(\frac{S_2}{S_1}\right)^{\alpha-1}, \alpha, \sigma_S\right) \quad (\text{G.6})$$

908 Transforming P_S into a function of ϵ with $\lambda_1 = -\ln(1 - \epsilon)/\Delta T$
 909 yields:

$$P_S(S|\epsilon, \alpha, \sigma_S) = C \prod_{i=1}^M p(S_i|\epsilon, \alpha, \sigma_{S,i}) = \frac{C}{\Delta T(1 - \epsilon)} \cdot \prod_{i=1}^M \left[\frac{1}{2\pi \sqrt{\sigma_{S,i}}} e^{-\frac{\left(S_i - S_2 \left(\frac{-\ln(1 - \epsilon)}{\Delta T \lambda_i}\right)^{1/(\alpha-1)}\right)^2}{2\sigma_{S,i}^2}} \right] \quad (\text{G.7})$$

910 Finally, P_S enters the joint posterior distribution from Eq. 2, that
 911 becomes

$$p(\epsilon, \alpha) = C \cdot (-\ln(1 - \epsilon))^M \cdot (\alpha - 1)^M \cdot \Gamma(\alpha) \left[\frac{(S_2/S_1)^{M+1}}{\pi} \right]^\alpha \cdot (1 - \epsilon)^{(T/\Delta T) \cdot (S_2/S_1)^{\alpha-1} - 1} \cdot P_S(S|\epsilon, \alpha, \sigma_S). \quad (\text{G.8})$$

912

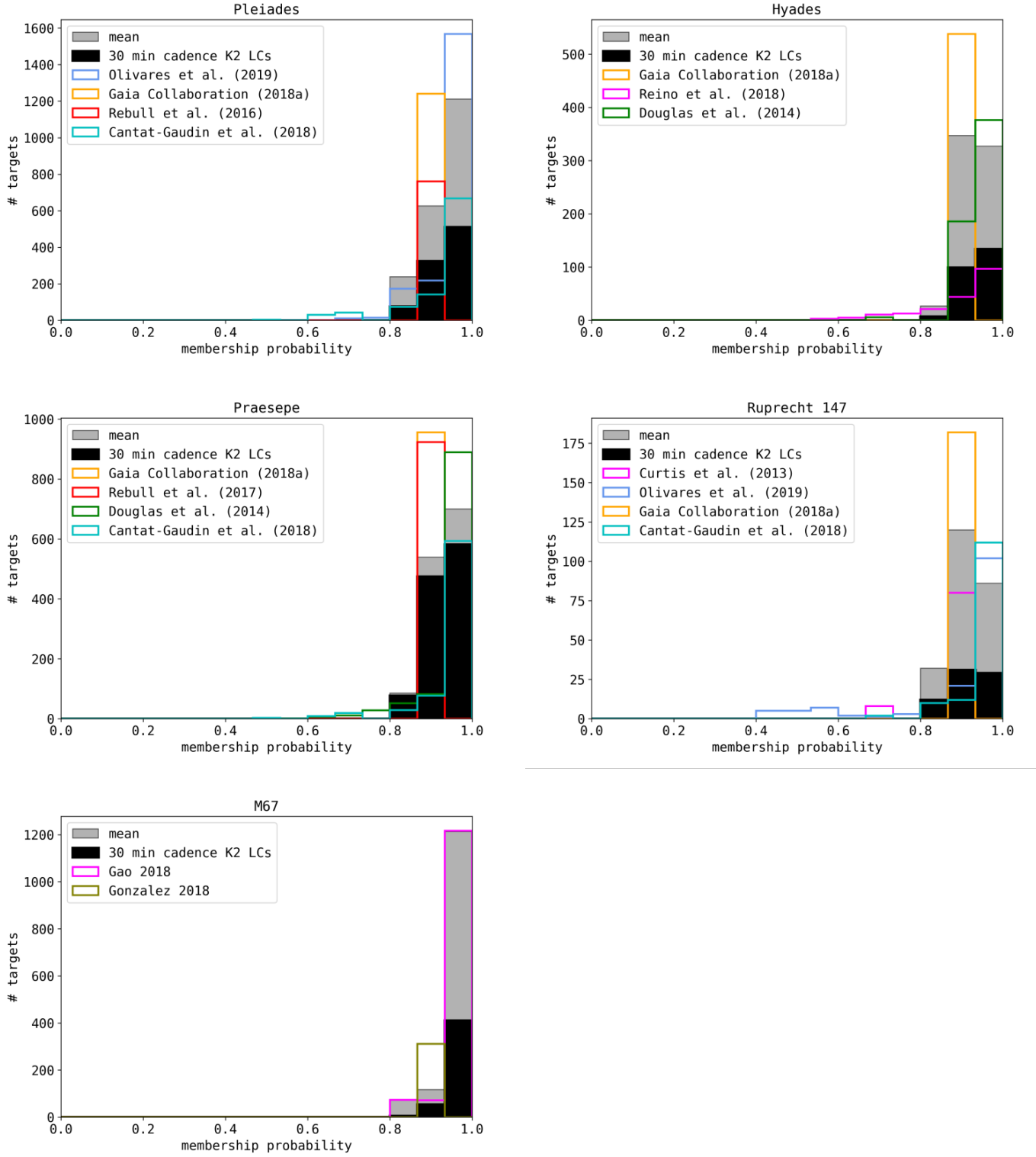


Fig. A.1. Membership histograms.

Table B.1. Non-exhaustive literature overview over OC parameters.

| cluster | source | distance [pc] | age [Myr] | [Fe/H] |
|-----------------|--|---------------|-------------------------|--------------------|
| Pleiades | adopted in this work: | 135.6 | $135 \pm_{25}^{25}$ | -0.037 ± 0.026 |
| Pleiades | Bossini et al. (2019) ^a | | $86.5 \pm_{2.4}^6$ | |
| Pleiades | Cantat-Gaudin et al. (2018) | 135.6 | | |
| Pleiades | Gossage et al. (2018) | | $135 \pm_{25}^{25}$ | |
| Pleiades | Yen et al. (2018) | 126.3 | $141.3 \pm_{100}^{170}$ | |
| Pleiades | Chelli and Duvert (2016) | 139 | | |
| Pleiades | Netopil et al. (2016) | | | -0.01 |
| Pleiades | Dahm (2015) | | $112 \pm_5^5$ | |
| Pleiades | Scholz et al. (2015) | 130 | 120 | |
| Pleiades | Conrad et al. (2014) | | | -0.037 ± 0.026 |
| Pleiades | Melis et al. (2014) | 136 | | |
| Pleiades | Bell et al. (2012) | 135 | 125 | |
| Hyades | adopted in this work:^c | | $690 \pm_{100}^{160}$ | 0.13 ± 0.02 |
| Hyades | Gaia Collaboration (2018) | | $690 \pm_{100}^{160}$ | |
| Hyades | Gossage et al. (2018) | | 680 | |
| Hyades | Liu et al. (2016) | | | ± 0.02 |
| Hyades | Netopil et al. (2016) | | | 0.13 |
| Hyades | Taylor and Joner (2005) | | | 0.103 ± 0.008 |
| Hyades | Cummings et al. (2005) | | | 0.146 ± 0.004 |
| Hyades | Salaris et al. (2004) | | 650 | 0.15 |
| Hyades | Perryman et al. (1998) | | $625 \pm_{50}^{50}$ | |
| Hyades | Martin et al. (1998) | | $650 \pm_{70}^{70}$ | |
| Praesepe | adopted in this work: | 185.5 | $750 \pm_7^3$ | 0.16 |
| Praesepe | Bossini et al. (2019) | | $750 \pm_7^3$ | |
| Praesepe | Cantat-Gaudin et al. (2018) | 185.5 | | |
| Praesepe | Gossage et al. (2018) | | 590 | |
| Praesepe | Yen et al. (2018) | 183 | $794 \pm_{269}^{253}$ | |
| Praesepe | Netopil et al. (2016) | | | 0.16 |
| Praesepe | Scholz et al. (2015) | 187 | 832 | |
| Praesepe | Boesgaard et al. (2013) | | | 0.12 |
| Praesepe | Boudreault et al. (2012) | 160 | 630 | |
| Praesepe | Salaris et al. (2004) | 175 | 650 | |
| Rup 147 | adopted in this work: | 305 | $2650 \pm_{380}^{380}$ | 0.08 ± 0.07 |
| Rup 147 | Bragaglia et al. (2018) | | | 0.08 ± 0.07 |
| Rup 147 | Cantat-Gaudin et al. (2018) | 305 | | |
| Rup 147 | Gaia Collaboration (2018) | 309 | $1995 \pm_{357}^{404}$ | |
| Rup 147 | Torres et al. (2018) | 283 | $2650 \pm_{380}^{380}$ | |
| Rup 147 | Curtis (2016) ^b | | | 0.10 ± 0.02 |
| Rup 147 | Scholz et al. (2015) | 270 | 1953 | |
| Rup 147 | Curtis et al. (2013) | 300 | $3125 \pm_{125}^{125}$ | 0.07 ± 0.03 |
| M67 | adopted in this work: | 908 | $3639 \pm_{17}^{17}$ | $-0.102 \pm .081$ |
| M67 | Bossini et al. (2019) | | $3639 \pm_{17}^{17}$ | |
| M67 | Netopil et al. (2016) | | | 0.03 |
| M67 | Scholz et al. (2015) | | $3428 \pm_{72}^{147}$ | |
| M67 | Conrad et al. (2014) | | | $-0.102 \pm .081$ |
| M67 | Dias et al. (2012) | 908 | 4300 | |
| M67 | Oñehag et al. (2011) | 880 | 4200 | 0.02 |

Notes. ^(a) Bossini et al. (2019) noted some caveats for their determination of ages of young clusters, for which they used Gaia DR2 photometry for isochrone fitting. ^(b) Curtis (2016) reanalysed HIRES spectra using an improved spectroscopic method as compared to Curtis et al. (2013). ^(c) We did not adopt a mean value for the Hyades distance because the cluster members are on average closer than 50 pc.

Table F.1. Literature overview over power law fitting approaches to FFDs.

| Who | method | data | $\alpha - 1$ |
|-------------------------|--|---|---------------------------------|
| Hawley et al. (2014) | LSq with Poisson uncertainty, increase the low energy limit until the fit is robust | | .95 (binned), 1.01 (cumulative) |
| Davenport (2016) | weighted LSq, asymmetric Poisson confidence intervals following Gehrels1986 | | |
| Gizis (2017) | de-biased MLE (Arnold2015), weight each point with \sqrt{N} in each bin (Clauset+2009) | 22 flares on one M7 UCD | .6-1. (31-33 erg) |
| Paudel et al. (2018) | ML from a paper in 2010, used emcee (Foreman-Mackey2013) | | |
| Lacy (1976) | graphical, linear LSq | 386 flares on UV Ceti | .43-1. |
| Güdel et al.(2003) | - | | |
| Davenport et al. (2012) | Fit $\log_{10} Y = \alpha + (\beta \log_{10} X)(10 - \gamma/(X + \delta))$ | ~50,000 M dwarfs from SDSS and 1321 M dwarfs from 2MASS | .9-2.1 |
| Lurie et al. (2015) | Bayesian Markov chain Monte Carlo based algorithm (Kelly 2007) for linear regression | 2 dMe5 dwarfs | .92-1.03 |
| Audard et al. (2000) | Crawford+1970 MLE (Jauncey-style) | EUVE 12 F-M type stars, 10-20 flares each | .46-1.61 |
| Shakhovskaia (1989) | linear representation, power laws from Gershberg/Shakhovskaya1983 | 30-40 dK0-dM8, 200 flares | .4-1.4 |
| Yang et al. (2017) | binned FFDs | 103187 flares on 540 M-type dwarfs in Kepler | 1.07 +/- 0.35 |
| Howard et al. (2018) | fit a cumulative power law, MCMC for uncertainties | 575 flares on 284 stars | 0.84-1.34 |
| Hilton et al. (2011) | | | .63-.83 |